Powder Technology 394 (2021) 44–61

Contents lists available at ScienceDirect

Powder Technology

journal homepage: www.elsevier.com/locate/powtec

Regimes of subsonic compressible flow in gas-particle systems

Jelena Mačak [a,b,*], Christoph Goniva [a], Stefan Radl [b]

[a] DCS Computing GmbH, 4020 Linz, Austria
[b] Graz University of Technology, Institute of Process and Particle Engineering, 8010 Graz, Austria

ARTICLE INFO

Article history:
Received 14 March 2021
Received in revised form 29 June 2021
Accepted 3 August 2021
Available online 10 August 2021

Keywords:
Compressible flow
Fixed and fluidized beds
Analytical solution
Verification
CFD-DEM

ABSTRACT

We present regime maps for subsonic flow in dense gas-particle systems, which demarcate regions of compressible and (effectively) incompressible flow. These maps should aid researchers and industrialists in selecting the appropriate modeling approach, as well as in verifying numerical solvers. Demonstrating compressibility at Mach numbers lower than 0.3, we show that this commonly used criterion is insufficient for flows in porous media. For $M < 0.1$, systems dominated by heat exchange experience compressible effects at a fixed value of a dimensionless system parameter, while critical parameters in an adiabatic system can be assessed using a simple relation of the Mach number. Ultimately, we present a model based on computational fluid dynamics and discrete element method (CFD-DEM) allowing efficient calculation of subsonic compressible gas-particle flows.

1. Introduction

Compressible flows are characterized by significant changes in gas density due to changes in pressure along the streamline. Three factors give rise to such flows: (i) friction, (ii) heat exchange, and (iii) changes in the cross-section area available for the gas flow. All three aforesaid factors are often found in typical gas-particle applications. Yet, in modeling of gas-particle flows, it is almost universally accepted to treat the gas phase as incompressible. The incompressibility assumption persisted because it simplifies the calculation, reducing the necessary computational resources. However, due to recent technological advances, it is possible today to carry out a comparably efficient simulation of pilot and even full-scale devices featuring particles and a compressible gas. This study shines a light on circumstances where it is necessary to treat the gas phase as compressible.

Next, we briefly review typical applications for compressible flow in gas-particle systems in Section 1.1, and the state-of-art modeling approaches in Section 1.2. Goals and limitations of the study are given in Section 1.3, and the study outline is documented in Section 1.4.

1.1. Overview of compressible gas-particle flows

Gas-particle flows occur under a variety of conditions, some of which add up to significant pressure-driven changes of gas density that render the flow compressible. Factors that cause such a flow include: (i) friction, i.e. the pressure drop caused by fluid-particle drag, (ii) heat exchange between the particles and the fluid, and (iii) changes of cross-sectional area due to variations in particle volume fraction.

Pneumatic conveying in long pipelines exemplifies a compressible flow caused by friction. Even under isothermal conditions, long distances allow frictional effects to add up to a pressure loss comparable to the absolute pressure at some reference point in the system. According to the ideal gas law, the ratio of pressure evens out with the density ratio. Therefore, large changes in pressure introduce large changes in density along the streamline. This can be experimentally observed by measuring the pressure along the pipeline length. While incompressible flow yields a linear pressure drop profile, deviations from linearity noted in long pipelines suggest compressible flow [1,2]. Other examples of friction-induced compressible gas flow include tall fluidized beds [3], and deep fluidized beds at low operating pressures [4,5]. Here mainly the weight of the particles (and hence frictional forces due to gas-particle slip) leads to pressure variations that are in the order of the absolute pressure in the system.

Heat exchange between the phases is inherent to many important industrial applications. For example, extreme heat release in chemical reactors [6] might lead to compressible flow. Another example is laser sintering [7], where melting particles heat up the ambient fluid, causing large local pressure and density variations.

Variations in particle volume fraction can also contribute to the compressibility of the system. In pneumatic conveying, particles tend to pile into dunes, forming wide channels down at the slopes, and narrow passages at the peaks. Additionally, spatial fluctuations of particle volume fraction are observed in almost all fluidized bed applications.

* Corresponding author at: DCS Computing GmbH, Industriezeile 35, 4020 Linz, Austria.
E-mail address: jelena.macak@dcs-computing.com (J. Mačak).

https://doi.org/10.1016/j.powtec.2021.08.017

1.2. State-of-art computational models

To calculate compressible gas-particle flows, it is typically necessary to resort to computational simulations. Popular state-of-art modeling approaches include the coupled computational fluid dynamics and discrete element method (CFD-DEM) [8], and the two fluid model (TFM) [9].

Major distinction between the two approaches is in the handling of the particle phase. In CFD-DEM, particles are seen as Lagrangian parcels. This allows descriptions of polydisperse granular materials, featuring cohesive interactions and particles of (almost) arbitrary shape. Due to advances in available computational power and coarse-graining techniques [10], CFD-DEM simulations are today applicable to pilot and full-scale devices. For example, it is possible to directly simulate long pneumatic conveying systems [11], or reactive systems with large temperature and pressure gradients [12]. Alternatively, in TFM, both particle and fluid phase are treated as continua, resulting in comparably low computational cost for dense systems.

While the present study uses CFD-DEM approach, our main findings are relevant also for other modeling approaches, such as the aforementioned TFM.

1.3. Goals and limitations

Even though gas-particle flows occur under a variety of conditions, widely used scaling-up techniques still indiscriminately rely on the assumption of incompressible gas flow [13,14]. While neglecting compressibility might lead to errors in some cases, to the best of our knowledge, no study identifies such cases with a simple and easy-to-use method or an equation. In classical gas dynamics, a commonly used criterion for compressible flow is the Mach number being above 0.3 [15]. However, in gas-particle systems compressibility effects are noted already at much lower velocities [1,2]. This calls for a careful consideration of relevant flow properties in these systems. Therefore, the main aim of this study is to provide means for identifying compressible gas-particle flows.

Specifically, the first goal of our study is to describe flow in gas-particle systems with pronounced compressibility of the gas phase using theoretical and computational tools.

The second goal is to find how system properties – such as device length, particle size, packing properties, gas properties, and heat release rate – relate to the compressibility of the flow. We do this by constructing dimensionless numbers that condense relevant system properties to a small set of non-dimensional influence parameters.

The third goal is to construct regime maps in terms of non-dimensional influence parameters which demarcate regions of compressible and incompressible flow. These maps are intended to aid researchers or industrialists in selection of the appropriate modeling approach, potentially preventing incorrect conclusions and thus saving precious resources.

The fourth and last goal is to demonstrate that an open-source CFD-DEM solver is able to predict these regimes as well, and hence allows expansion of our conclusion to general (i.e., three dimensional) situations in the future.

Although interest in sonic gas-particle flows is emerging [16–18], we limit our current analysis to subsonic flows. The major focus of our present study is the distinction between flows we consider incompressible and compressible. Since sonic flows are by default compressible, our limitation to subsonicity is naturally implied.

We also limit our present study to a fixed gas-phase composition and a perfect gas (i.e., validity of the ideal gas law and a constant heat capacity are assumed). This is motivated by the fact that we can derive analytical solutions for such a gas. Extension to variable composition, or even to a real gas is possible using the numerical solution approach presented here.

In the theoretical model, we also exclude effects due to gravity, since they do not contribute more than marginally to pressure fluctuations. Again, for a more rigorous analysis of gas-particle suspensions, gravity can be included in the CFD-DEM model.

1.4. Outline

In Section 2, we start our analysis by defining compressible flow. Next, we name the factors that cause compressible flow, i.e., all relevant phenomena causing changes in gas density are discussed. We follow by deriving a set of differential equations describing one-dimensional flow through a packed bed, and finish this section by describing a CFD-DEM model, which can be used for advanced physical modeling of gas-particle flows and arbitrarily complex geometries.

In Section 3 we classify and describe subsonic flow regimes found in gas-particle systems. The regimes are classified according to the dominant factor that causes density changes in the system. In Section 3.1 we provide analytical solutions for all relevant flow properties (i.e., density, pressure, temperature, velocity) if only one of these factors is present. Specifically, these regimes are (i) flow with friction caused by gas-particle drag (Section 3.2), (ii) flow with heat exchange (Section 3.3), and (iii) flow in a channel with a change in packing density, i.e., a spatially-variable particle volume fraction (Section 3.5). Additionally, since friction cannot be neglected in gas-particle systems, we present combined regimes: flow with heat exchange and friction (Section 3.4), as well as flow with change in packing density and friction (Section 3.6). For each of the regimes we provide a map delineating regions of compressible and (effectively) incompressible flow. The maps can be used for a quick selection of the appropriate modeling approach, as shown in Section 3.2.2, where we determine whether clustering in fluidized beds will be affected by the compressibility of the gas phase. We also test the validity of the isothermal flow assumption, and provide the maps extended with boundaries of isothermal and non-isothermal region.

We summarize our findings and recommendations in Section 4.

2. Mathematical model

In the following section, we document mathematical models for a pressure-driven compressible gas flow through a static bed of particles. We first mathematically define what we understand as *incompressible* and *compressible*, by quantifying the corresponding changes in gas density. Next the three factors which cause this density change are described: (i) friction (pressure losses due to gas-particle drag), (ii) heat exchange, and (iii) change of the particle volume fraction. To understand the influence of each of these factors, we derive a set of differential equations describing one-dimensional flow in a particle bed. Finally, we briefly describe a more rigorous CFD-DEM-based model, which can be used for advanced physical modeling of gas-particle flows.

2.1. Definition of the compressible flow

Compressible flow is tied to compressibility, property of a fluid to change its volume under applied change in pressure. From the mathematical standpoint, compressible flows are described with equations that account for variable density. In theory, every flow could be correctly described with such equations. However, due to the increase in computational effort, mathematical models with variable density are reserved for flows where density changes significantly along the streamline.

Considering relative change of inlet and outlet gas densities defined as:

$$\Delta_\rho \equiv \frac{|\rho_{\text{in}} - \rho_{\text{out}}|}{\rho_{\text{out}}}, \tag{1}$$

we quantify the significant density change using the following limits:

$$\begin{aligned} \Delta_\rho &< 10\% \quad \Rightarrow \quad \text{incompressible flow,} \\ \Delta_\rho &> 25\% \quad \Rightarrow \quad \text{compressible flow.} \end{aligned} \tag{2}$$

According to the definition above, we consider the flow incompressible if the relative change of density in the system stays below 10%, and compressible if the change is above 25%. For the relative changes between the two limits, flow regime selection depends on the required precision of the solution.

It is worth noting here, that not every flow with large change in density is compressible. According to [19], there is a distinction between low-Mach number variable density flows and compressible flows. Former is characterized by density variations arising due to composition and temperature variations, while density variations in the latter are pressure-driven. Flow regimes presented in this study feature pressure-driven density changes, and thus fall under compressible flow category. However, we demonstrate existence of compressible flows even at arbitrary low Mach numbers (assuming the continuum hypothesis holds).

Additionally, we test the validity of the isothermal flow assumption. Defining the relative temperature change in the system as:

$$\Delta_T \equiv \frac{|T_{\text{in}} - T_{\text{out}}|}{T_{\text{out}}}, \tag{3}$$

we will, similar as before, adopt the following limits for considering the flow isothermal:

$$\begin{aligned} \Delta_T &< 10\% \quad \Rightarrow \quad \text{isothermal flow,} \\ \Delta_T &> 25\% \quad \Rightarrow \quad \text{non} - \text{isothermal flow.} \end{aligned} \tag{4}$$

2.2. Factors causing compressible flow

Classical gas dynamics identifies three factors that cause a compressible flow: (i) friction, (ii) heat exchange, and (iii) change of cross-sectional area available for fluid flow. Considering compressible, one-dimensional flow through a pipe, analytical solutions exist for special cases featuring only one of the three aforementioned factors. These are respectively: (i) the Fanno regime, describing adiabatic viscous flow; (ii) the Rayleigh regime, describing inviscid flow with heat exchange; and (iii) the isentropic regime, describing adiabatic inviscid flow in pipes with a variable cross-sectional area [20]. Equivalent factors can be found in gas flow through a particle bed.

In an empty pipe, friction will occur at the rough pipe walls. In a packed bed, particles will resist the flow by obstructing the passage and by increasing the amount (i.e., area) of rough surface the fluid adheres to. Therefore, by friction we will refer to the collective influence of particle drag and wall friction as in pipe flow.

Heat exchange occurs if particles and gas are at different temperatures, for example due to an external heat influx, such as from a laser [7], or from a chemical reaction [6]. We consider heating if particles are at a higher temperature than the ambient gas, and cooling in the opposite case.

In a single-phase gas flow, changes in cross-sectional area instigate changes in gas density because the flow accelerates (or decelerates), meaning that temperature and pressure must change as well. The cross-sectional area might decrease as in the case of a converging nozzle, or increase as in a diverging diffuser. Hence, variations in particle volume fraction in a gas-particle system will cause an equivalent gas behaviour as the variations in cross-sectional area in a single-phase flow. The nozzle flow regime will occur if the particle volume fraction increases in the main flow direction, while the diffuser flow regime will occur if the particle volume fraction decreases in the flow direction. While the void space between particles is more complex in shape compared to a nozzle considered in classical gas dynamical calculations, we consider this complexity to only affect frictional losses.

2.3. Compressible flow in a one-dimensional static particle bed

To lay the ground for describing compressible flow in a particle bed, we start from the known gas dynamical relations describing flow in an empty pipe. The flow is steady and one-dimensional, with gradients only occurring in the x-direction, parallel to the pipe axis. The pipe length is denoted as L. The fluid is a perfect gas, and body forces are neglected. The pipe is heated, features a gradual change of cross-sectional area A, and, since the fluid is viscous, friction occurs at the pipe walls. Due to the aforementioned phenomena, the gas will bear a change in pressure p, velocity u, temperature T and density ρ between the inlet and outlet.

If we consider a differential length element dx, the governing equations for mass, momentum and energy transport are, respectively [15]:

$$\frac{\mathrm{d}\rho}{\rho} + \frac{\mathrm{d}u}{u} + \frac{\mathrm{d}A}{A} = 0, \tag{5}$$

$$\rho u \,\mathrm{d}u + \mathrm{d}p = -\mathrm{d}F, \tag{6}$$

$$c_{p,f}\mathrm{d}T + u\mathrm{d}u = \mathrm{d}q. \tag{7}$$

In the equations above, dA is the differential change of the cross-sectional area, dF is the differential frictional force, dq is the differential rate of heat transfer through the pipe wall, and $c_{p,f}$ is the specific heat capacity of the fluid, assumed to be constant. Additionally, the ideal gas law relates flow properties to the gas constant R:

$$p = \rho \mathrm{R}\ \mathrm{T}. \tag{8}$$

The ideal gas law can be also written in a more useful differential form:

$$\frac{\mathrm{d}\rho}{\rho} + \frac{\mathrm{d}T}{T} - \frac{\mathrm{d}p}{p} = 0. \tag{9}$$

The above equations can be used to describe flow through porous media, such as in the particle bed shown in Fig. 1. We will additionally assume that the pipe hosting the particle bed has a constant cross-sectional area (this assumption can be easily relaxed by considering a more complex expression for dA as discussed below), and that the particles are spherical with a common diameter d_p.

2.3.1. Mass balance

The mass balance equation for flow through a particle bed will differ from the one used for flow in an empty pipe, Eq. (5), in two ways: (1) it will feature a change of packing density instead of the change of the cross-sectional area; (2) it will feature the

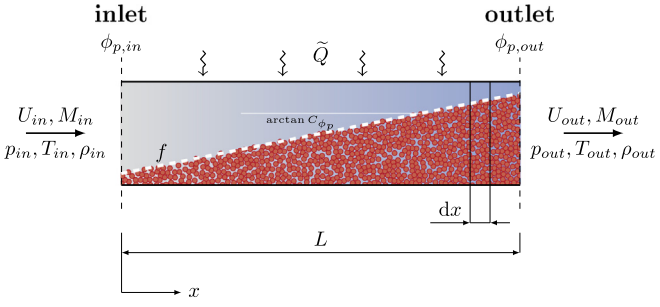

Fig. 1. One-dimensional compressible flow with friction, heat exchange, and a linear change of particle volume fraction in a static particle bed.

superficial gas velocity instead of the interstitial (i.e., phase-average) gas velocity.

In a packed bed, the change of cross-sectional area available for gas flow will be related to the change of the particle volume fraction φ_p. The cross section change will hence be equivalent to the change in the voidage $1-\varphi_p$:

$$\frac{\mathrm{d}A}{A}=\frac{\mathrm{d}\left(1-\varphi_p\right)}{1-\varphi_p}. \tag{10}$$

We now assume a linear change of particle volume fraction (or equivalently the voidage) as schematically illustrated in Fig. 1:

$$(1-\varphi_p)_x=C_0+C_{\varphi_p}\frac{x}{d_p}, \tag{11}$$

where x is the axial coordinate, the constant $C_0=(1-\varphi_p)_{x=0}$ equals the voidage at the inlet, and C_{φ_p} is the dimensionless slope of the voidage profile.

For $C_{\varphi_p}<0$ the voidage is decreasing, and the flow will be as through a converging nozzle. This nozzle-like configuration is depicted in Fig. 1. For $C_{\varphi_p}>0$ the voidage is increasing, and the flow will be as through a diverging diffuser. In the rest of the text, we will additionally use the following definition for a more concise documentation of the results: $\widetilde{C}\equiv C_{\varphi_p}/C_0$.

In a particle bed, it is beneficial to use the superficial gas velocity U instead of the true gas velocity u:

$$U\equiv(1-\varphi_p)u, \tag{12}$$

The superficial gas velocity represents the fluid velocity that would be acquired in an empty pipe of equivalent cross-section. The mass balance Eq. (5) for a particle bed thus becomes:

$$\frac{\mathrm{d}\rho}{\rho}+\frac{\mathrm{d}U}{U}=0. \tag{13}$$

Losses in momentum that occur due to tortuosity of the void space between the particles will be accounted for in the friction force, which is discussed next.

2.3.2. Momentum balance

The momentum balance takes into account frictional effects due to viscous dissipation in the gas phase and momentum losses due to tortuosity of the void space between the particles. For example, using Ergun's closure for pressure drop in a dense bed of particles [21], one calculates the friction coefficient from:

$$f=\left(1.75+150\frac{\varphi_p}{\mathrm{Re}}\right)\frac{\varphi_p}{1-\varphi_p}. \tag{14}$$

In the above formulation, viscous losses are inversely proportional to the particle Reynolds number:

$$\mathrm{Re}=\frac{\rho U d_p}{\mu}, \tag{15}$$

where μ is the dynamic viscosity of the gas.

The differential friction force per unit cross-sectional area acting on the differential length dx is thus:

$$\mathrm{d}F=f\frac{\rho u^2}{d_p}\mathrm{d}x. \tag{16}$$

We express the momentum balance in a dimensionless form using the Mach number:

$$M^2=\frac{u^2}{\kappa \mathrm{RT}}=\frac{\rho u^2}{\kappa p}. \tag{17}$$

The Mach number scales the gas velocity with the speed of sound $\sqrt{\kappa \mathrm{RT}}$, where κ is the isentropic exponent.

Using the above definitions, the differential momentum balance Eq. (6) for a gas flowing through a particle bed becomes:

$$\frac{\mathrm{d}U}{U}+\frac{1}{\kappa M^2}\frac{\mathrm{d}p}{p}=-f\frac{\mathrm{d}x}{d_p}+\frac{\mathrm{d}A}{A}. \tag{18}$$

2.3.3. Energy balance

A fluid mass-specific differential amount of heat dq appears in the energy balance Eq. (7). We assume that this amount of heat is exchanged between the gas and the particles within the length increment dx, and no other heat sources or sinks (e.g., due to a chemical reaction) are present in the gas phase. Consequently, dq is related to the heat exchange rate per m^3 of fluid $\dot{q}_f$ as follows:

$$\mathrm{d}q=\frac{\dot{q}_f\mathrm{d}x}{\rho u}. \tag{19}$$

We find that $\dot{q}_f$ is related to the rate of heat per unit particle volume $\dot{q}_p$ that is lost by the particles:

$$\dot{q}_f=-\frac{\varphi_p}{1-\varphi_p}\dot{q}_p. \tag{20}$$

The heat exchange rate per m^3 of particles is closed by the expression:

$$\dot{q}_p=\alpha(T-T_p)\frac{A_p}{V_p}, \tag{21}$$

where α is the heat transfer coefficient. For spherical particles, the volume-specific surface area is:

$$\frac{A_p}{V_p}=\frac{6d_p^2\pi}{d_p^3\pi}=\frac{6}{d_p}. \tag{22}$$

We estimate the heat transfer coefficient α using:

$$\alpha=\frac{\lambda_f \mathrm{Nu}}{d_p}, \tag{23}$$

where *Nu* is the Nusselt number (expressing the ratio of the exchanged heat flux and a typical conductive heat flux in a fluid), and λ_f is the heat conductivity of the fluid. According to Gunn [22], the Nusselt number in a dense particle bed can be estimated as a function of voidage $(1-\varphi_p)$, particle Reynolds number *Re* and Prandtl number *Pr*:

$$\begin{aligned}\mathrm{Nu}=&\left(7-10(1-\varphi_p)+5(1-\varphi_p)^2\right)\left(1+0.7\mathrm{Re}^{0.2}\mathrm{Pr}^{1/3}\right)\\&+\left(1.33-2.4(1-\varphi_p)+1.2(1-\varphi_p)^2\right)\mathrm{Re}^{0.7}\mathrm{Pr}^{1/3}.\end{aligned} \tag{24}$$

Using the relations $c_{p,f}/R=\kappa/(\kappa-1)$, $Pr=c_{p,f}\mu/\lambda_f$, and the definitions of the Mach and Reynolds number, respectively Eqs. (17) and (15), the energy equation becomes:

$$\frac{\mathrm{d}T}{T}+(\kappa-1)M^2\frac{\mathrm{d}U}{U}=\widetilde{Q}\frac{\mathrm{d}x}{d_p}+(\kappa-1)M^2\frac{\mathrm{d}A_\varphi}{A_\varphi}, \tag{25}$$

with the dimensionless heating coefficient defined as:

$$\widetilde{Q}=\frac{6\varphi_p \mathrm{Nu}}{\mathrm{Pr}\ \mathrm{Re}}\left(\frac{T_p}{T}-1\right). \tag{26}$$

2.3.4. Summary of the governing equations

Fluid flow through a particle bed is fully described by Eqs. (9), (13), (18) and (25). This equation set can be re-written in terms of 4 variables, respectively pressure p, superficial gas velocity U, gas temperature T, and gas density ρ as follows:

$$\begin{aligned}
\frac{\mathrm{d}p}{p} &= -\frac{\kappa M^2\left(1+(\kappa-1)M^2\right)}{1-M^2} f\frac{\mathrm{d}x}{d_p} - \frac{\kappa M^2}{1-M^2}\widetilde{Q}\frac{\mathrm{d}x}{d_p} + \frac{\kappa M^2}{1-M^2}\frac{\mathrm{d}A}{A} \\
\frac{\mathrm{d}U}{U} &= \frac{\kappa M^2}{1-M^2} f\frac{\mathrm{d}x}{d_p} + \frac{1}{1-M^2}\widetilde{Q}\frac{\mathrm{d}x}{d_p} - \frac{M^2}{1-M^2}\frac{\mathrm{d}A}{A} \\
\frac{\mathrm{d}T}{T} &= -\frac{\kappa(\kappa-1)M^4}{1-M^2} f\frac{\mathrm{d}x}{d_p} + \frac{1-\kappa M^2}{1-M^2}\widetilde{Q}\frac{\mathrm{d}x}{d_p} + \frac{(\kappa-1)M^2}{1-M^2}\frac{\mathrm{d}A}{A} \\
\frac{\mathrm{d}\rho}{\rho} &= -\frac{\kappa M^2}{1-M^2} f\frac{\mathrm{d}x}{d_p} - \frac{1}{1-M^2}\widetilde{Q}\frac{\mathrm{d}x}{d_p} + \frac{M^2}{1-M^2}\frac{\mathrm{d}A}{A}.
\end{aligned} \tag{27}$$

The above system of ordinary differential equations can be solved numerically, e.g., using a Runge-Kutta integrator. When knowing the friction coefficient f, the heating coefficient $\widetilde{Q}$, and the voidage distribution (and hence dA), integration can be carried out forwards (i.e., from inlet to outlet) or backwards (i.e., from outlet to inlet). Forward integration requires knowing the state at the inlet, i.e., at $x = 0$: p_{in}, U_{in}, T_{in}, ρ_{in}, M_{in}, while backward integration requires the state at the outlet, i.e., at $x = L$: p_{out}, U_{out}, T_{out}, ρ_{out}, M_{out}. The equationshave a singularity at $M = 1$. This is the transition point from subsonic to sonic flow, where the fluid moves faster than the speed of sound.

An additional important relation emerges from the differentiation of the definition of the Mach number, i.e., Eq. (17), combined with the above governing equations:

$$\begin{aligned}
\frac{\mathrm{d}M^2}{M^2} &= \frac{\mathrm{d}\rho}{\rho} + 2\frac{\mathrm{d}U}{U} - 2\frac{\mathrm{d}\left(1-\varphi_p\right)}{1-\varphi_p} - \frac{\mathrm{d}p}{p} \\
&= \frac{2\kappa M^2\left(\frac{\kappa-1}{2}M^2+1\right)}{1-M^2}\cdot f\frac{\mathrm{d}x}{d_p} + \frac{\kappa M^2+1}{1-M^2}\cdot\widetilde{Q}\frac{\mathrm{d}x}{d_p} \\
&\quad - \frac{2\left(\frac{\kappa-1}{2}M^2+1\right)}{1-M^2}\cdot\frac{\mathrm{d}A}{A}
\end{aligned} \tag{28}$$

The above equation is the basis for analytical solutions, which can be derived when isolating the influences of friction, heat exchange, and variable particle volume fraction.

2.4. CFD-DEM model with a compressible fluid phase

A full three-dimensional description of a gas-particle flow calls for numerical modeling techniques. The numerical model presented here uses a combined computational fluid dynamics and discrete element method (CFD-DEM)-based approach.

The solution algorithm starts by calculating position and forces of every particle using the DEM. Discrete particle data is then averaged and mapped onto an Eulerian grid to arrive at a continuum-like field description of the particles. In this step, forces from particles to the fluid, such as drag, are calculated and added to fluid's continuum-based equations. Finally, fluid fields are calculated using a pressure-based algorithm. Note that when following such a procedure we are unable to resolve the exact gas-particle interface. Hence we speak of an unresolved CFD-DEM approach.

The model is implemented in the software CFDEMCoupling [8,23]. For particle calculations we use LIGGGHTS [24,25], and as the basis for the fluid flow solution we use OpenFOAM [26–28].

2.4.1. Summary of governing equations

A detailed description of the CFD-DEM procedure and the associated governing equations can be found in a large number of references [8, 29–31]. In addition to the equation of state Eq. (8), flow of a compressible fluid is described using the mass balance equation:

$$\frac{\partial\left(\left(1-\varphi_p\right)\rho\right)}{\partial t} + \nabla\cdot\left(\left(1-\varphi_p\right)\rho\mathbf{u}\right) = 0, \tag{29}$$

the momentum balance equation:

$$\frac{\partial\left(\left(1-\varphi_p\right)\rho\mathbf{u}\right)}{\partial t} + \nabla\cdot\left(\left(1-\varphi_p\right)\rho\mathbf{u}\mathbf{u}\right) - \nabla^2(\mu\mathbf{u}) = -\nabla p + \mathbf{f}_{\mathrm{pf}}, \tag{30}$$

and the energy balance equation:

$$\begin{aligned}
&\frac{\partial(\left(1-\varphi_p\right)\rho h)}{\partial t} + \nabla\cdot\left(\left(1-\varphi_p\right)\mathrm{u}h\right) \\
+\quad &\frac{\partial(\left(1-\varphi_p\right)\rho k)}{\partial t} + \nabla\cdot\left(\left(1-\varphi_p\right)\mathrm{u}k\right) + \frac{\partial p}{\partial t} - \nabla^2(\alpha_{\mathrm{eff}}h) = \dot{q}_{\mathrm{pf}}.
\end{aligned} \tag{31}$$

For the sake of brevity, the equations presented here are stripped-down of terms that equate to zero when applied to our simulation setups. This includes terms due to temporal change of void fraction and terms due to particle velocity. We also note here that the above formulation is valid for deeply subsonic flows, up to $M = 0.1$. Sonic and even transonic flows, call for different mathematical and numerical treatment, as discussed in [31,18].

In Eq. (29) the fluid velocity is denoted by the vector $\mathbf{u}$, ρ is the fluid density, and φ_p is the particle volume fraction. Quantity $1 - \varphi_p$ is the void fraction, i.e. porosity. The particle volume fraction indicates how much of the CFD-cell volume is occupied by the particle phase. Since the test cases in our study feature regular (i.e., each particle is fully enclosed by a single fluid cell) and static packings (see Fig. 2), the particle volume fraction is calculated using the simple and efficient particle centre method (PCM) [32]. In general, CFD-DEM simulations feature irregular particle arrangements of moving particles, and PCM might lead to large temporal fluctuations of the particle volume fraction in individual fluid cells. For such more general situations it is hence recommended to use the divided scheme for estimation of the particle volume fraction [30,33].

The momentum balance Eq. (30) contains the pressure term p, the stress term $\nabla^2(\mu\mathbf{u})$ (typically of negligible importance in case of gas-particle systems), and the force term $\mathbf{f}_{pf}$ which models all relevant particle-fluid interactions. One of such interactions is the drag force particles exert onto the fluid. For the CFD-DEM simulations, we used the drag closure of Koch-Hill [34]. However, it is important to note here that the conclusions of the study are insensitive to the specific drag model used, as long as the drag coefficient does not depend on the Mach number. Thus, our results could also be predicted with a closure such as that of Ergun [21], Di Felice [35], or Gidaspow [36]. As mentioned, an exception would be a drag model that takes (in addition to the Reynolds number and particle volume fraction) the local Mach number into account. Although such models exist for isolated spheres [37–39], we are only aware of first attempts to develop such a drag model [40]. Hence, it is inconclusive how an advanced Mach number-based model would alter our main conclusions.

The energy balance Eq. (31) contains the specific enthalpy $h = c_{p,f}T$, the specific kinetic energy $k = |\mathbf{u}^2|/2$, and heat conduction modelled with an effective heat diffusivity α_{eff}. The specific heat exchange rate between the fluid and the particles $\dot{q}_{\mathrm{pf}}$ is described with the following expression:

$$\dot{q}_{\mathrm{pf}} = \alpha(T - T_{p,\mathrm{avg}})a_{\mathrm{pc}}, \tag{32}$$

where α is the heat exchange coefficient, a_{pc} is the volume-specific surface area of the particle cloud within a computational cell, and $T_{p,avg}$ is the average temperature of the particles in the cell. The heat transfer coefficient is expressed with Eq. (23), which calls for

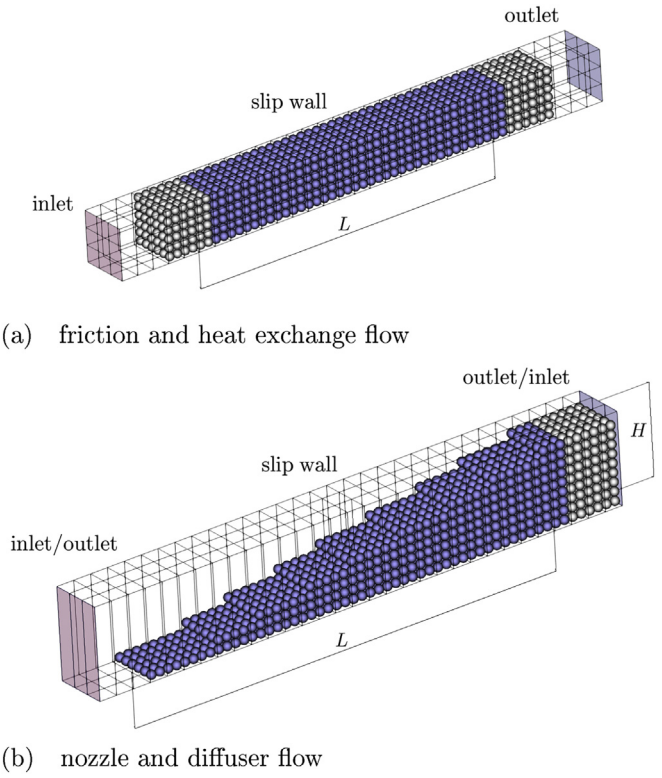

Fig. 2. The simulation domains. Results are sampled over the length L occupied by the blue-colored particles. For friction and heat exchange regimes (a), the cells are cubic with side length of 2 particle diameters. For nozzle and diffuser regimes (b), the cells are of height H. In the nozzle regime, the inlet is at the cross-section devoid of particles. In the diffuser regime, the inlet is at the cross-section with the highest packing density.

a closure such as that of Gunn [22], i.e., Eq. (24). The temperature of an individual particle is obtained through the particle-based energy balance equation:

$$\rho_p c_p \frac{\partial T_p}{\partial t} = \dot{q}_p + \dot{q}_s, \tag{33}$$

where ρ_p is the particle density, c_p specific heat capacity of the particle, $\dot{q}_p$ is the rate of heat exchange between fluid and particles per unit particle volume, and $\dot{q}_s$ is an external heat source imposed on the particles per unit particle volume, for example from a laser.

We note in passing that our CFD-DEM solver can additionally model gravity, rotating meshes, radiation, and user-defined source terms which are not discussed in detail here since they are not relevant in our present study.

2.4.2. Simulation setup

We will examine the following situations:

1. **Flow with friction**: flow is adiabatic (no particle-fluid heat exchange) and the particle volume fraction is constant along the bed length.
2. **Flow with heat exchange**: the particle volume fraction is constant along the bed length, while particles exchange heat with the fluid.
3. **Flow with change in particle volume fraction**: flow is adiabatic and the particle volume fraction changes linearly across the bed length.

The domain depicted in Fig. 2a is used for the flow with friction and the flow with heat exchange, while the domain in Fig. 2b is used for flow with change in particle volume fraction. Simulations of flow with heat exchange, and flow with change in particle volume fraction both have friction: the fluid is viscous and there is particle drag. This is necessary, since friction dampens numerical oscillations caused by changes in void fraction that would otherwise cause unphysical results. For simulations using the domain shown in Fig. 2a, we cut off a length of 6 particle diameters in the main direction at each side, and sampled results only over the length denoted as L. This is to avoid spurious velocity oscillations caused by steep changes of void fraction [41]. Each CFD cell is cubical and of identical size in Fig. 2a, with an edge length of two particle diameters.

Table 1
Boundary conditions imposed on the fluid in the CFD-DEM simulations.

	Inlet	Outlet	Wall
Pressure	Zero gradient	Fixed value	Zero gradient
Velocity	Fixed value	Zero gradient	Slip
Temperature	Fixed value	Zero gradient	Zero gradient

For simulations considering the change in particle volume fraction, a pseudo-2D domain is used. The width and the length of each cell is two particle diameters, while there is only one cell over the height H (i.e., we consider a height-averaged form of the governing equations). In the converging nozzle regime, the inlet is completely devoid of particles. Linearly progressing across the bed length L, the maximum packing is reached at the outlet. In the diverging diffuser regime, the inlet and outlet switch positions: the inlet features the maximum packing density, while the outlet is completely devoid of particles. For postprocessing, results are sampled over the length L. Similar configuration is also used in [16–18] to verify compressible flow at high Mach numbers.

The boundary conditions imposed at the fluid are summarized in Table 1.

Friction and heat coefficients as they appear in Eq. (27) should be constant along the bed length to make the equations integrable. In a CFD-DEM simulation, this is generally not the case. Friction results from the employed drag law, and heat transfer from Nusselt correlations. Both are affected by the fluid and particle properties at the local cell level. Thus, to verify the CFD-DEM solution, Runge-Kutta integration is carried out step-wise, using friction and heat coefficient calculated from simulation properties harvested at the local cell.

2.4.3. Physical parameters

Unless otherwise stated, we used particle and fluid properties as in Table 2.

3. Results

Compressible flow in a gas-particle system might be provoked by friction, heat exchange, and/or by change in particle volume fraction. If only one of the three aforementioned factors is present, there is an analytical solution to the one-dimensional model documented in the previous chapter. However, this solution has a direct application only for the flow with friction, which comprises pressure losses due to gas-particle drag. In real world applications, the other two factors inducing compressibility always appear in connection with friction. Hence, we investigate the following flows:

Table 2
Fluid and particle properties used in flow simulations.

Property	Value
Dynamic viscosity	$\mu = 1 \times 10^{-5}\,\mathrm{Pa \cdot s}$
Gas constant	$R = 287.1 \frac{\mathrm{J}}{\mathrm{kgK}}$
Isentropic exponent	$\kappa = 1.4\ (-)$
Fluid specific heat capacity	$c_{p,f} = 1007 \frac{\mathrm{J}}{\mathrm{kgK}}$
Particle diameter	$d_p = 0.001$ m
Particle volume fraction	$\varphi_p \approx 0.5\ (-)$
Inlet temperature	$T_{in} = 1000$ K
Particle temperature	$T_p = 1000$ K

- Flow with friction;
- Flow with heat exchange;
- Flow with heat exchange and friction;
- Flow with change in particle volume fraction;
- Flow with change in particle volume fraction and friction.

For each of these we provide a regime map, spanned by dimensionless numbers, that separates regions of compressible and (almost) incompressible flow.

3.1. Analytical solutions to compressible gas-particle flow

Compressible flow in a one-dimensional static particle bed is described by Eq. (27). The equation set features three factors affecting the compressibility of the system: friction, heat exchange, and change in particle volume fraction, each quantified respectively with: f, $\widetilde{Q}$, and $\mathrm{d}A$. If any two of the aforementioned factors are set to zero, Eqs. (28) and (27) can be integrated from inlet at $x = 0$ (subscript *in*) towards the outlet at $x = L$ (subscript *out*). This procedure leads to three solutions. First solution is found for flow with friction ($f = \text{const.}\neq 0, \widetilde{Q} = 0, \mathrm{d}A = 0$):

$$\begin{aligned}
f\frac{L}{d_p} &= \frac{\kappa+1}{4\kappa}\ln\left(\frac{M_{\text{in}}^2}{M_{\text{out}}^2}\cdot\frac{\frac{\kappa-1}{2}M_{\text{out}}^2+1}{\frac{\kappa-1}{2}M_{\text{in}}^2+1}\right)+\frac{M_{\text{out}}^2-M_{\text{in}}^2}{2\kappa M_{\text{in}}^2 M_{\text{out}}^2},\\
\frac{p_{\text{in}}}{p_{\text{out}}} &= \frac{M_{\text{out}}}{M_{\text{in}}}\sqrt{\frac{\frac{\kappa-1}{2}M_{\text{out}}^2+1}{\frac{\kappa-1}{2}M_{\text{in}}^2+1}},\\
\frac{U_{\text{in}}}{U_{\text{out}}} &= \frac{M_{\text{in}}}{M_{\text{out}}}\sqrt{\frac{\frac{\kappa-1}{2}M_{\text{out}}^2+1}{\frac{\kappa-1}{2}M_{\text{in}}^2+1}},\\
\frac{T_{\text{in}}}{T_{\text{out}}} &= \frac{\frac{\kappa-1}{2}M_{\text{out}}^2+1}{\frac{\kappa-1}{2}M_{\text{in}}^2+1},\\
\frac{\rho_{\text{in}}}{\rho_{\text{out}}} &= \frac{M_{\text{out}}}{M_{\text{in}}}\sqrt{\frac{\frac{\kappa-1}{2}M_{\text{in}}^2+1}{\frac{\kappa-1}{2}M_{\text{out}}^2+1}}.
\end{aligned} \tag{34}$$

The above solution assumes a friction coefficient.

Second solution is found for flow with heat exchange ($\widetilde{Q} = \text{const.}\neq 0, f = 0, \mathrm{d}A = 0$):

$$\begin{aligned}
\widetilde{Q}\frac{L}{d_p} &= \ln\left(\frac{M_{\text{out}}^2}{M_{\text{in}}^2}\cdot\left(\frac{\kappa M_{\text{in}}^2+1}{\kappa M_{\text{out}}^2+1}\right)^{\frac{\kappa+1}{\kappa}}\right)\\
\frac{p_{\text{in}}}{p_{\text{out}}} &= \frac{\kappa M_{\text{out}}^2+1}{\kappa M_{\text{in}}^2+1},\\
\frac{U_{\text{in}}}{U_{\text{out}}} &= \frac{M_{\text{in}}^2}{M_{\text{out}}^2}\cdot\frac{\kappa M_{\text{out}}^2+1}{\kappa M_{\text{in}}^2+1},\\
\frac{T_{\text{in}}}{T_{\text{out}}} &= \frac{M_{\text{in}}^2}{M_{\text{out}}^2}\cdot\left(\frac{\kappa M_{\text{out}}^2+1}{\kappa M_{\text{in}}^2+1}\right)^2,\\
\frac{\rho_{\text{in}}}{\rho_{\text{out}}} &= \frac{M_{\text{out}}^2}{M_{\text{in}}^2}\cdot\frac{\kappa M_{\text{in}}^2+1}{\kappa M_{\text{out}}^2+1}.
\end{aligned} \tag{35}$$

Finally, the third solution is found for flow with change in particle volume fraction ($\mathrm{d}A = \text{const.}\neq 0, f = 0, \widetilde{Q} = 0$):

$$\begin{aligned}
\frac{A_{\text{out}}}{A_{\text{in}}} = \widetilde{C}\frac{L}{d_p}+1 &= \frac{M_{\text{in}}}{M_{\text{out}}}\cdot\sqrt{\left(\frac{\frac{\kappa-1}{2}M_{\text{out}}^2+1}{\frac{\kappa-1}{2}M_{\text{in}}^2+1}\right)^{\frac{\kappa+1}{\kappa-1}}}\\
\frac{p_{\text{in}}}{p_{\text{out}}} &= \left(\frac{\frac{\kappa-1}{2}M_{\text{out}}^2+1}{\frac{\kappa-1}{2}M_{\text{in}}^2+1}\right)^{\frac{\kappa}{\kappa-1}}\\
\frac{U_{\text{in}}}{U_{\text{out}}} &= \left(\frac{\frac{\kappa-1}{2}M_{\text{in}}^2+1}{\frac{\kappa-1}{2}M_{\text{out}}^2+1}\right)^{\frac{1}{\kappa-1}},\\
\frac{T_{\text{in}}}{T_{\text{out}}} &= \frac{\frac{\kappa-1}{2}M_{\text{out}}^2+1}{\frac{\kappa-1}{2}M_{\text{in}}^2+1}\\
\frac{\rho_{\text{in}}}{\rho_{\text{out}}} &= \left(\frac{\frac{\kappa-1}{2}M_{\text{out}}^2+1}{\frac{\kappa-1}{2}M_{\text{in}}^2+1}\right)^{\frac{1}{\kappa-1}}.
\end{aligned} \tag{36}$$

Here we assume a linear change of particle volume fraction, i.e. $\mathrm{d}A = \mathrm{d}\left(1-\varphi_p\right) = C_{\varphi_p}\mathrm{d}x/d_p$, and introduce parameter $\widetilde{C}\equiv C_{\varphi_p}/C_0$ for brevity (see Section 2.3.1).

Fig. 3 illustrates possible profiles of flow properties, according to the analytical relations presented here.

Fig. 3a shows how flow properties change in a subsonic flow with friction. Friction always increases the entropy of the system, implying that the friction coefficient is always larger than zero ($f > 0$). In a particle-fluid system, friction is due to fluid viscosity and particle drag. Particles act as obstacles which fluid can only overcome by accelerating towards the outlet. The needed acceleration manifests as an increase in velocity and Mach number. Consequently, sufficient pressure drop must exist to support the velocity change. Due to the continuity constraint, density change is inversely proportional to the velocity change. Following the ideal gas law, if both density and pressure drop, temperature drops as well. However, since no heat is added to the system, temperature changes only slightly. Proof that the flow in the friction regime is effectively isothermal is given in Section 3.2.1. In Fig. 3a, Eq. (34) was calculated using friction coefficient $f = 1$, for flow accelerating from $M_{in} = 0.01$ to $M_{out} = 0.1$. Comparing the analytical solution to a Runge-Kutta-based numerical integration of Eq. (27) yields a maximum relative difference of 0.03%, and a mean relative difference of 0.01%.

In contrast to the subsonic flow with friction which can only accelerate, subsonic flow with heat exchange accelerates if heated ($\widetilde{Q}>0$) and decelerates if cooled ($\widetilde{Q}<0$). Fig. 3b illustrates heated flow in red, and cooled flow in blue. Adding heat increases the energy levels in the system. An increase in kinetic energy is equivalent to an increase in velocity and Mach number. Consequently, pressure and density will drop. Temperature rises with added heat, however, only up until the Mach number reaches $M = 1/\sqrt{\kappa}$. Afterwards, the temperature drops even though the fluid is still heated. For Mach numbers $1/\sqrt{\kappa}<M<1$, the required velocity increase is such that the internal energy has to drop to appease the acceleration. If the fluid is cooled, the opposite changes take place. The velocity and the Mach number drop when moving into the flow direction, while pressure and density rise. The temperature rises in the range $1>M>1/\sqrt{\kappa}$, and falls for $M<1/\sqrt{\kappa}$. In Fig. 3b, Eq. (35) is calculated using $\widetilde{Q} = 0.001$ for heating, and $\widetilde{Q} = -0.001$ for cooling. In both cases, minimum Mach number in the system is $M_{min} = 0.7$ and the maximum Mach number is $M_{max} = 1$. This range is chosen to capture the maximum point in the temperature profile. The solution is compared against results of a Runge-Kutta-based numerical integration of Eq. (27). The comparison yields maximum

relative difference of 2.4e− 5 % for heating, and 0.004% for cooling. Mean relative difference is 3.3e− 6 % for heating, and 5.5e− 4 % for cooling.

Subsonic flow with linear change in particle volume fraction is shown in Fig. 3c. Increasing the particle volume fraction ($\widetilde{C}<0$) decreases the space available for fluid flow. This is an equivalent situation to fluid flow through a nozzle, where acceleration is achieved due to cross-section reduction. While velocity and Mach number rise, pressure, temperature, and density drop as shown in Fig. 3c in red. The opposite case, where particle volume fraction decreases ($\widetilde{C}>0$), results in a diffuser-like flow: velocity and Mach number drop, while pressure, density and temperature rise, as shown in Fig. 3c in blue. Trends depicted in Fig. 3c, are calculated from Eq. (36) with the Mach number ranging from $M_{min} = 0.35$ to $M_{max} = 1$, and with the normalized slope of $\widetilde{C} = -0.005$ in nozzle regime and $\widetilde{C} = 0.005$ in diffuser regime. Comparing the analytical solution Eq. (36) against a Runge-Kutta-based integration of Eq. (27) yields a maximum relative difference of 0.008%, and a mean relative difference of 8.4e− 5 % for nozzle flow, as well as a maximum relative difference of 0.01%, and a mean relative difference of 0.001% for diffuser flow.

For all presented cases, discrepancies between the analytical and the Runge-Kutta-based numerical solution stayed below 0.05%. This verifies the suitability of the Runge-Kutta-based numerical integrator for describing flows with more than one non-zero compressibility-related factor. While flow with friction as described in Eq. (34) might be applied to a real gas-particle system, frictionless flows as in Eqs. (35) and (36) are only hypothetical. Friction due to fluid-particle drag generally cannot be neglected, and will appear in conjunction with other compressibility-related factors. However, before introducing friction, it is necessary to understand how isolated factors affect the changes in flow properties. Hence, we first present regime maps based on analytical predictions only, and then study the effects of adding friction. The regime maps demarcate regions of (effectively) incompressible and compressible flow, as well as (effectively) isothermal and non-isothermal regions where applicable.

3.2. Flow with friction

We construct a regime map with regions of compressible and incompressible flow, for one-dimensional flow with friction (gas-particle drag) in a static packed bed. Flow is deemed compressible if the overall

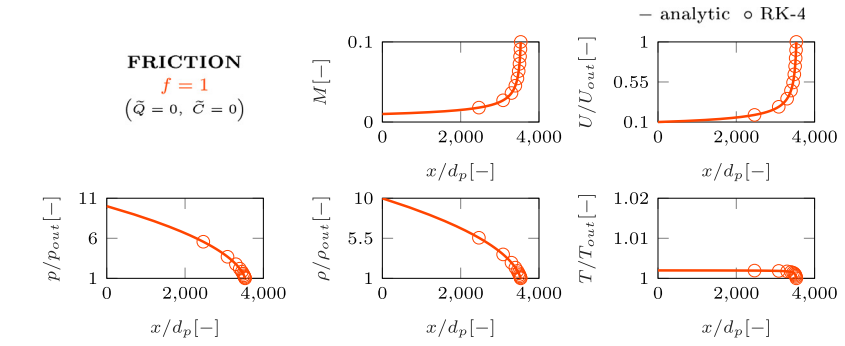

(a) Flow with friction

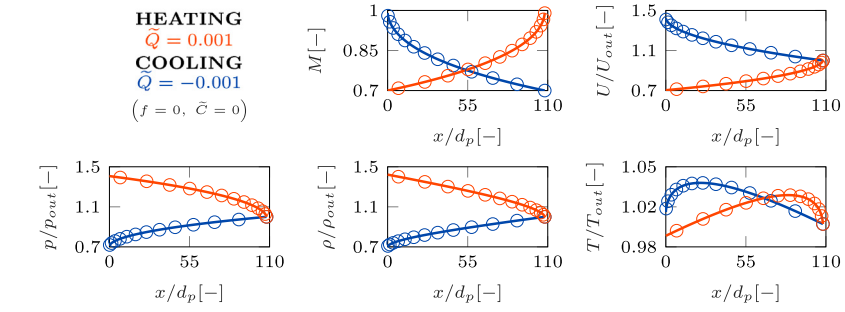

(b) Flow with heat exchange

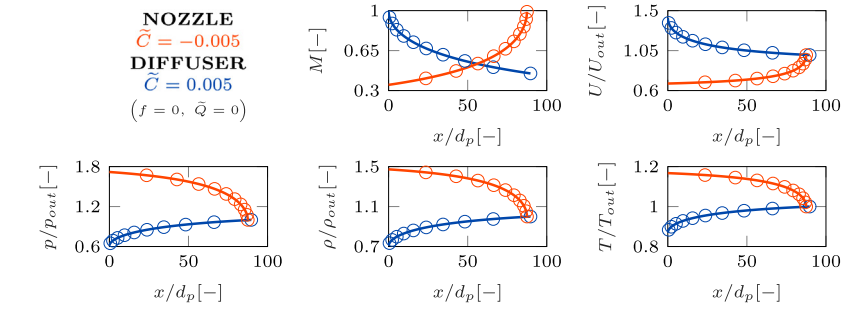

(c) Flow with change in particle volume fraction

Fig. 3. Changes of flow properties along the bed length in flow with friction (a), frictionless flow with heat exchange (b), and frictionless flow with change in particle volume fraction (c).

relative change of gas density is larger than 25%. For changes lower than 10%, flow is considered incompressible.

To overcome friction, the flow accelerates towards the outlet. The outlet state is thus characterized by the maximum Mach number $M_{out} = M_{max}$, while the minimum Mach number characterizes the state at the inlet $M_{in} = M_{min}$. Assuming the outlet state is known, and denoting the density ratio as $\rho_{in}/\rho_{out} = \delta_\rho$, we can derive the following relation from Eq. (34):

$$f\frac{L}{d_p} = \frac{\left(\frac{\kappa-1}{2}M_{\max}^2+1\right)\left(\delta_\rho^2-1\right)}{2\kappa M_{\max}^2} - \frac{\kappa+1}{2\kappa}\ \ln\delta_\rho. \tag{37}$$

The equation is physical for $\rho_{in} > \rho_{out} \Rightarrow \delta_\rho > 1$, implying that the density will decrease along the flow direction. A similar procedure can be followed if the inlet state is known, resulting in:

$$f\frac{L}{d_p} = \frac{\frac{\kappa-1}{2}M_{\min}^2+1}{2\kappa M_{\min}^2}\cdot\frac{\delta_\rho^2-1}{\delta_\rho^2} - \frac{\kappa+1}{2\kappa}\ \ln\delta_\rho. \tag{38}$$

The above equation describes subsonic flow only until the corresponding outlet Mach number reaches $M_{out} = M_{max} = 1$. This is essentially a choking condition, similar to isentropic flow in a converging nozzle [20].

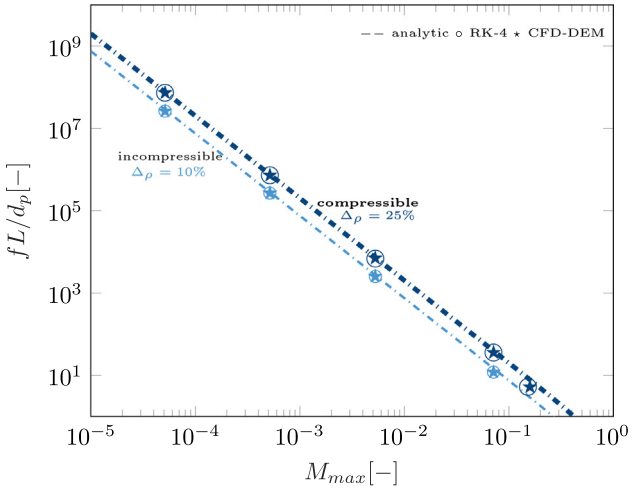

(a) based on the maximum Mach number

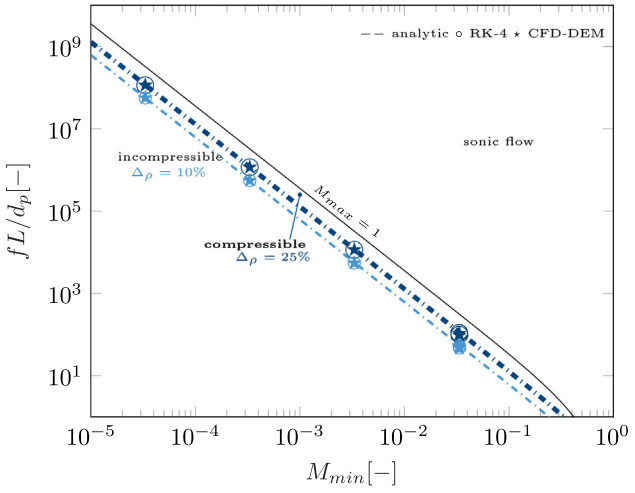

(b) based on the minimum Mach number

Fig. 4. Regime map for flow with friction.

The regime map plotted with the maximum Mach number is shown in Fig. 4a. Boundaries for the incompressible and compressible flow region are obtained by setting δ_ρ in Eq. (37) to 1.1 and 1.25 respectively. The regime map for flow with friction based on a minimum Mach number is shown in Fig. 4b. Boundaries for compressible and incompressible flow are calculated as before, using $\delta_\rho = 1.1$ and $\delta_\rho = 1.25$ in Eq. (38). The map has an additional line indicating sonic flow, calculated using the choking condition $M_{out} = M_{max} = 1$ in Eq. (34).

The axis fL/d_p in Fig. 4 will have the low limit for the combination of the lowest friction factor f and the lowest bed length to particle diameter ratio L/d_p. Using Ergun's friction closure [21], the lowest friction coefficient is for the Reynolds number tending to infinity:

$$f = \lim_{\mathrm{Re}\to\infty}\left(\left(1.75+150\frac{\varphi_p}{\mathrm{Re}}\right)\frac{\varphi_p}{1-\varphi_p}\right) = 1.75\frac{\varphi_p}{1-\varphi_p}. \tag{39}$$

Considering dilute flows with $\varphi_p = 0.1$ in the relation above, the lowest possible friction factor is in order of magnitude of $2\varphi_p$. The absolutely shortest meaningful pipe length is one particle diameter. Thus, the lowest theoretical frictional length can be set to $(f\ L/d_p)_{\min} \approx 2\varphi_p$, assuming very high Reynolds number, very dilute flow, and a very short pipe. Hence, we will consider the lower limit for the frictional length to be 1 in our figures. All real-world particle-fluid systems will have a frictional length above this limit.

According to Fig. 4, compressible boundary intersects the lowest frictional length at approximately $M = 0.3$, which is the traditionally adopted criterion for compressible flow. This confirms that flow around a single sphere becomes compressible at $M = 0.3$. However, when systems of particles are considered, the compressible effects arise at much lower velocities. Specifically, for subsonic velocities with $M_{max} < 0.1$, the ln-term in Eq. (37) is negligibly small. Using $\kappa = 1.4$ and $\delta_\rho = 1.25$, a simple relation between the maximum Mach number and the system parameter fL/d_p emerges:

$$\left(5\left(f\frac{L}{d_p}\right)_{\Delta\rho=25\%} - \frac{1}{5}\right)M_{\max}^2 = 1. \tag{40}$$

For $M_{max} = 0.1$, the above approximate relation produces 0.51% relative error compared to Eq. (37). This error is even smaller for lower Mach numbers.

Similar approximate relationship can be found for the minimum Mach number, by neglecting the ln-term in Eq. (38), and using $\kappa = 1.4$ and $\delta_\rho = 1.25$ as before:

$$\left(7.78\left(f\frac{L}{d_p}\right)_{\Delta\rho=25\%} - \frac{1}{5}\right)M_{\min}^2 = 1. \tag{41}$$

Compared to Eq. (38), the relation above produced relative error of 1.6% for $M_{min} = 0.1$. Same as before, the error reduces for decreasing Mach numbers. Therefore, at low Mach numbers, compressibility of the system can be assessed using the following criteria:

$$\begin{aligned}\left(5f\frac{L}{d_p}-\frac{1}{5}\right)M_{\max}^2 &> 1,\\ \left(7.78f\frac{L}{d_p}-\frac{1}{5}\right)M_{\min}^2 &> 1.\end{aligned} \tag{42}$$

If any of the above conditions is true, it is very likely that the flow will be compressible.

The map shown in Fig. 4 is verified using Runge-Kutta integration of Eq. (27) and CFD-DEM simulations. We used fluid and particle properties as defined in Table 2. The domain used for the CFD-DEM simulations is as shown in Fig. 2a. We ran 5 simulation setups, with boundary conditions as defined in Table 3.

All setups were run with Courant number $Co = 100$, attesting the efficiency of the solution. The highest relative error of 5.5% was observed

Table 3
Setups used in friction flow simulations.

Simulation	p_{out} (Pa)	U_{in} (m/s)	L/d_p (−)	M_{in} (−)	M_{out} (−)	$\bar{f}$ (−)
1	10,000	10	200	0.034	0.155	1.4
2	100,000	10	200	0.033	0.072	1.3
3	10,000	1	1000	0.003	0.005	20
4	10,000	0.1	10,000	3e−4	5e−4	185
5	100	0.01	1000	3e−5	5e−5	2e5

for simulation setup 1. Simulation setup 1 also reaches the highest Mach number $M_{out} = 0.16$, which is the practical application limit for a low-speed, pressure-based CFD algorithm as used by us. Mean relative error for all simulation setups equals 0.48%.

3.2.1. Proof that flow with friction is effectively isothermal

If we express Eq. (34) in terms of the temperature ratio $T_{in}/T_{out} = \delta_T$, and the outlet ($M_{out} = M_{max}$) or the inlet state ($M_{in} = M_{min}$), we end up with, respectively:

$$f\frac{L}{d_p} = \frac{\kappa+1}{4\kappa}\ln\left(\frac{\frac{\kappa-1}{2}M_{\max}^2+1-\delta_T}{\frac{\kappa-1}{2}M_{\max}^2}\right) + \frac{(\delta_T-1)\left(\frac{\kappa-1}{2}M_{\max}^2+1\right)}{2\kappa M_{\max}^2\left(\frac{\kappa-1}{2}M_{\max}^2+1-\delta_T\right)}, \tag{43}$$

and

$$f\frac{L}{d_p} = \frac{\kappa+1}{4\kappa}\ln\left(\frac{\delta_T\frac{\kappa-1}{2}M_{\min}^2}{\delta_T\left(\frac{\kappa-1}{2}M_{\min}^2+1\right)-1}\right) + \frac{(\delta_T-1)\left(\frac{\kappa-1}{2}M_{\min}^2+1\right)}{2\kappa\left(\delta_T\left(\frac{\kappa-1}{2}M_{\min}^2+1\right)-1\right)}. \tag{44}$$

The argument of the ln function must be strictly positive, which is always true for:

$$1<\delta_T<\frac{\kappa-1}{2}M_{\max}^2+1. \tag{45}$$

For the maximum outlet Mach number of $M_{max} = 1$, the maximum temperature ratio is $\delta_{T,max} = 1.2$, meaning that the subsonic friction regime will never become non-isothermal if we adopt 25% as the limit according to Eq. (4). The change of temperature reaches 10% only in high transonicity, at $M_{max} \approx 0.7$, and for subsonic velocities with $M < 0.1$ the temperature ratio effectively equals 1, confirming that a flow with friction is effectively isothermal.

3.2.2. Will compressibility affect clustering in a fluidized bed?

The friction flow model can be applied to conclude whether compressibility affects clustering in fluidized beds. We derived the model for fixed beds, where particle positions are locked. However, the same model can be applied to a situation where both particles and fluid move, considering the fluid-particle relative velocity. The typical velocity in a fluidized bed is the sedimentation speed of an isolated particle, known as terminal settling velocity u_t:

$$u_t = \sqrt{\frac{3}{4}\frac{(\rho_p-\rho)gd_p}{\rho C_D}}. \tag{46}$$

The drag coefficient C_D can be expressed using the Schiller-Naumann relation [42]:

$$C_D = \frac{24}{\mathrm{Re}}\cdot\left(1+0.15\mathrm{Re}^{0.687}\right). \tag{47}$$

In a fluidized bed, an important length scale is the one where inertial forces balance out the gravitational forces [43,44]:

$$L = \frac{u_t^2}{g}. \tag{48}$$

This length scale can be considered a typical cluster length scale, i.e., the typical size of dense regions in an otherwise comparably dilute background flow. A closure for friction in fluidized beds is given by [45]:

$$f_{\text{Beetstra}} = \frac{18\varphi_p(1-\varphi_p)}{\mathrm{Re}}\cdot\left(\frac{10\varphi_p}{(1-\varphi_p)^2}+(1-\varphi_p)^2\left(1+1.5\varphi_p^{1/2}\right) + \frac{0.413\mathrm{Re}}{24(1-\varphi_p)^2}\cdot\frac{(1-\varphi_p)^{-1}+3\varphi_p(1-\varphi_p)+8.4\mathrm{Re}^{-0.343}}{1+10^{3\varphi_p}\mathrm{Re}^{-(1+4\varphi_p)/2}}\right). \tag{49}$$

We assume that, in a fluidized bed, one might find:

- particles with density ρ_p of 2000 $\frac{\mathrm{kg}}{\mathrm{m}^3}$, and with diameter d_p ranging from 10μm to 1000μm;
- a particle volume fraction φ_p ranging from 0.1 to 0.5;
- air as a working fluid at pressure p ranging from 1kPa to 500kPa, and at temperature T ranging from 300K to 2000K.

Selecting a combination of values from above allows us to calculate the velocity and bed length scale using Eqs. (46) and (48), as well as the

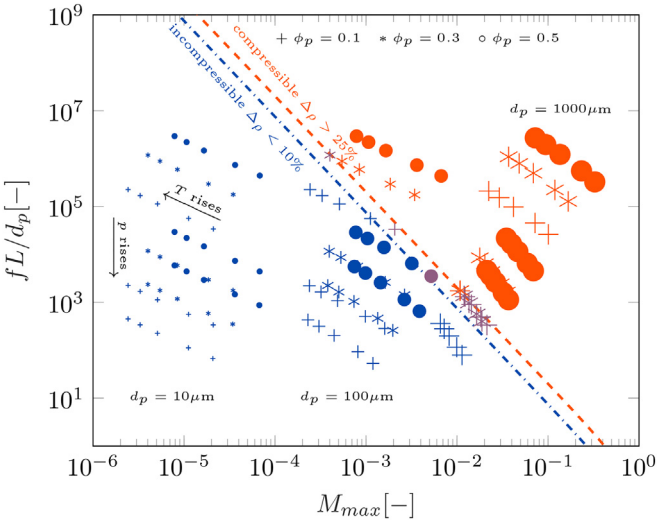

Fig. 5. Flow regimes in fluidized beds. Size of the symbols indicates the particle size. Different symbols indicate different particle volume fraction. For identical symbols an increase in temperature is indicated when moving from left to right, and an increase in pressure when moving from bottom to top.

Table 4
Properties of frictionless flow with heat exchange.

	Heating	Cooling
Heat coefficient	$\tilde{Q}>0$	$\tilde{Q}<0$
Maximum Mach number	$M_{max} = M_{out}$	$M_{max} = M_{in}$
Minimum Mach number	$M_{min} = M_{in}$	$M_{min} = M_{out}$
Compressible flow limit	$\delta_\rho = 1.25$	$\delta_\rho = 0.75$
Incompressible flow limit	$\delta_\rho = 1.1$	$\delta_\rho = 0.9$
Non-isothermal flow limit	$\delta_T = 0.75$	$\delta_T = 1.25$
Isothermal flow limit	$\delta_T = 0.9$	$\delta_T = 1.1$

maximum Mach number M_{max} and friction coefficient f using Eq. (49). This allows us to indicate each combination in the friction regime map (Fig. 5).

The map above reveals that large particle diameters, and dense packings are more likely to show pronounced compressibility effects. Also, for a commonly-used particle size of 100μm, compressibility effects need to be considered already at the cluster scale, at least for some combinations of pressure and temperature. In addition, for large-scale fluidized bed applications the relevant process-scale length is typically much larger than $L = u_t^2/g$, and hence compressibility effects need to be expected much earlier than shown in Fig. 5.

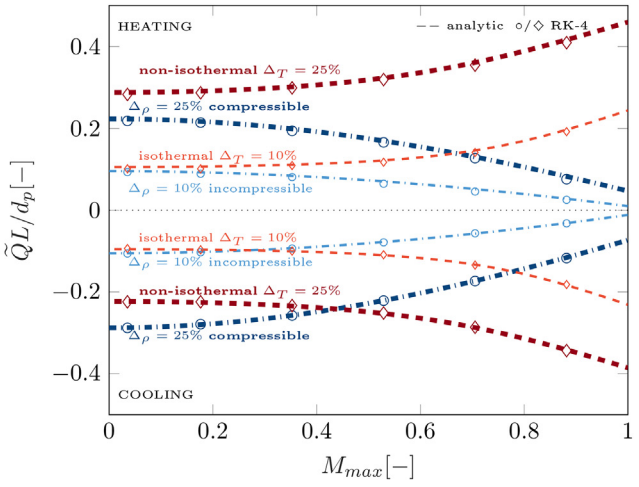

(a) based on the maximum Mach number

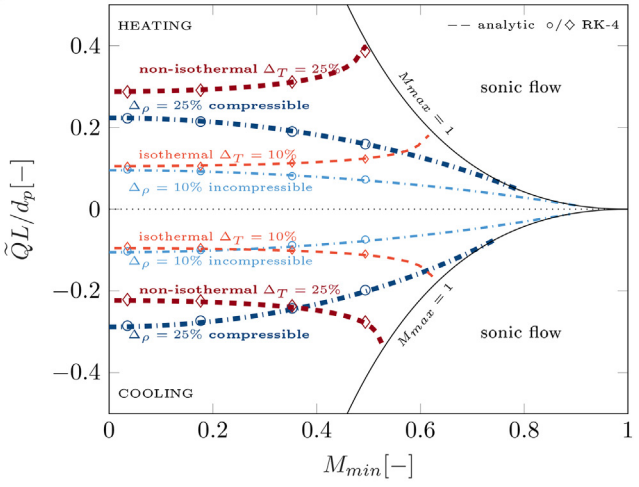

(b) based on the minimum Mach number

Fig. 6. Regime map for frictionless flow with heat exchange.

3.3. Flow with heat exchange

We construct a regime map with regions of compressible and incompressible flow, as well as isothermal and non-isothermal flow, for a one-dimensional frictionless flow with heat exchange in a static packed bed. Depending whether the flow is heated or cooled, the flow will have the features as summarized in Table 4.

Using Eq. (35), the density ratio $\rho_{in}/\rho_{out} = \delta_\rho$ can be related to the parameter $\tilde{Q}L/d_p$. If the outlet or inlet state is known, we can derive from Eq. (35), respectively:

$$\tilde{Q}\frac{L}{d_p} = \ln\left(\frac{\delta_\rho^{\kappa+1}}{\kappa M_{\text{out}}^2(\delta_\rho - 1) + \delta_\rho}\right)^{\frac{1}{\kappa}}, \tag{50}$$

or

$$\tilde{Q}\frac{L}{d_p} = \ln\left(\delta_\rho \cdot \left(\kappa M_{\text{in}}^2(1-\delta_\rho) + 1\right)^{\frac{1}{\kappa}}\right). \tag{51}$$

Similarly, Eq. (35) can be expressed in terms of the temperature ratio $T_{in}/T_{out} = \delta_T$. Considering the outlet (M_{out}) or the inlet (M_{in}) Mach number, we arrive at the following equations, respectively:

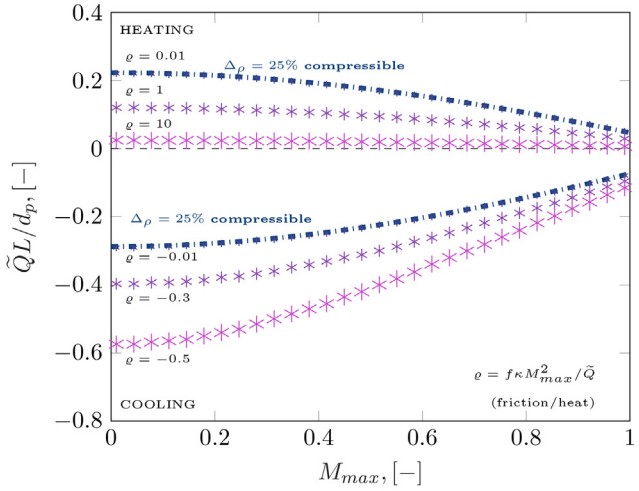

(a) based on the maximum Mach number

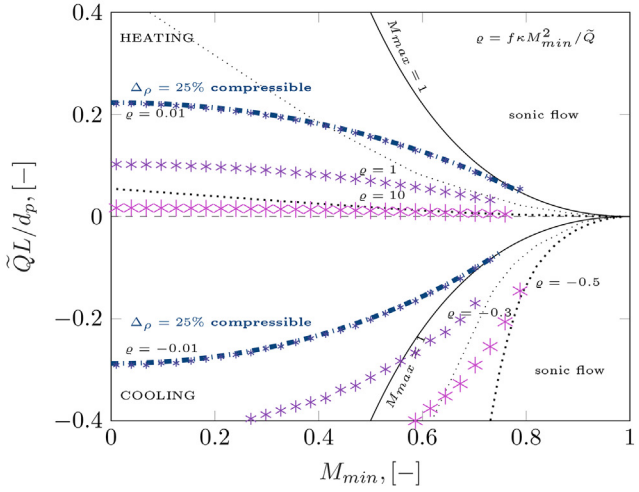

(b) based on the minimum Mach number

Fig. 7. Regime map with compressible flow regions in flow with heat exchange and friction.

$$\widetilde{Q}\frac{L}{d_p} = \ln\left[\frac{2\kappa^2 M_{\text{out}}^4\delta_T}{-2\kappa M_{\text{out}}^2\delta_T + \left(\kappa M_{\text{out}}^2+1\right)^2 \pm \left(\kappa M_{\text{out}}^2+1\right)\sqrt{\left(\kappa M_{\text{out}}^2+1\right)^2 - 4\kappa M_{\text{out}}^2\delta_T}} \cdot \left(\frac{\left(\kappa M_{\text{out}}^2+1\right) \pm \sqrt{\left(\kappa M_{\text{out}}^2+1\right)^2 - 4\kappa M_{\text{out}}^2\delta_T}}{2\kappa M_{\text{out}}^2\delta_T}\right)^{\frac{\kappa+1}{\kappa}}\right], \tag{52}$$

and

$$\widetilde{Q}\frac{L}{d_p} = \ln\left[\frac{-2\kappa M_{\text{in}}^2 + \left(\kappa M_{\text{in}}^2+1\right)^2\delta_T \pm \left(\kappa M_{\text{in}}^2+1\right)\sqrt{\left(\left(\kappa M_{\text{in}}^2+1\right)^2\delta_T - 4\kappa M_{\text{in}}^2\right)\delta_T}}{2\kappa^2 M_{\text{in}}^4} \cdot \left(\frac{2\kappa M_{\text{in}}^2}{\left(\kappa M_{\text{in}}^2+1\right)\delta_T \pm \sqrt{\left(\left(\kappa M_{\text{in}}^2+1\right)^2\delta_T - 4\kappa M_{\text{in}}^2\right)\delta_T}}\right)^{\frac{\kappa+1}{\kappa}}\right]. \tag{53}$$

The quadratic dependence in Eq. (35) leads to positive and negative roots in the above relations. To test the validity of the isothermal flow assumption, we used only the negative roots. Also, the above equations are valid only for positive parameters of the square root and ln function.

We use the relations Eqs. (50)–(53) along with the definitions in Table 4 to construct regime maps linked to maximum and minimum Mach number, shown respectively in Fig. 6a and b. Boundaries of the effectively incompressible flow and the compressible flow regions are plotted using respectively light blue and dark blue dash-dotted lines, while the respective boundaries of the effectively isothermal and the non-isothermal region are plotted using light red and dark red dashed lines. The map linked to the minimum Mach number has additional continuous lines denoting the transition to sonic flow. These lines can be constructed by using the chocking condition $M_{max} = 1$ in Eq. (35).

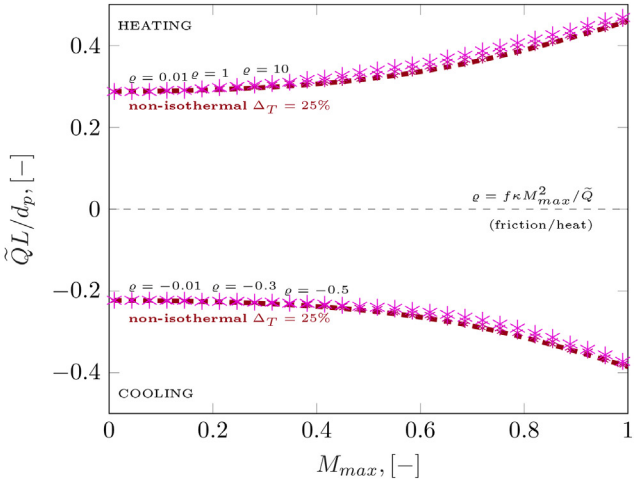

(a) based on the maximum Mach number

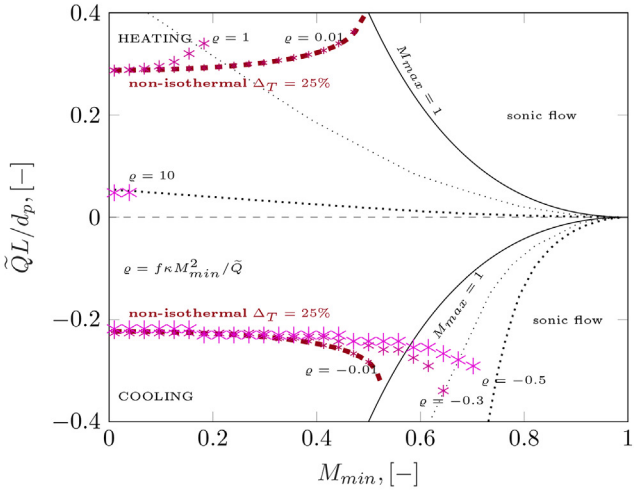

(b) based on the minimum Mach number

Fig. 8. Regime map with non-isothermal flow regions in flow with heat exchange and friction.

It can be seen in Fig. 6, that for the increasing Mach number the compressible region tends to expand, while the non-isothermal region tends to reduce. This means that for a higher Mach number, the same change in density will appear at comparably lower values of $\widetilde{Q}L/\mathrm{dp}$, while the same change in temperature will appear at higher values of $\widetilde{Q}L/\mathrm{dp}$. It is important to note that at lower velocities (i.e., $M < 0.2$), the boundaries remain almost constant, allowing us to derive the following simple criteria for such comparably slow frictionless flows:

$$\begin{aligned} |\widetilde{Q}|L/d_p &< 0.1 \quad \Rightarrow \text{incompressibleandisothermal},\\ \widetilde{Q}L/d_p &> 0.2 \quad \Rightarrow \text{compressibleheating},\\ \widetilde{Q}L/d_p &> 0.3 \quad \Rightarrow \text{non}-\text{isothermalheating},\\ \widetilde{Q}L/d_p &< -0.2 \quad \Rightarrow \text{non}-\text{isothermalcooling},\\ \widetilde{Q}L/d_p &< -0.3 \quad \Rightarrow \text{compressiblecooling}. \end{aligned} \tag{54}$$

We note here that, as shown in the following section, adding friction up to $\varrho = 0.1$ will not significantly shift the compressibility-related boundaries, while isothermal region is not significantly affected by friction.

3.4. Flow with heat exchange and friction

Since friction should not be neglected in any gas-particle system, we study how friction combined with heat exchange affects the compressibility. Setting the change of particle volume fraction to zero in Eq. (27), the gas density change is a follows:

$$\frac{\mathrm{d}\rho}{\rho} = -\frac{\kappa M^2}{1-M^2} f\frac{\mathrm{d}x}{d_p} - \frac{1}{1-M^2}\widetilde{Q}\frac{\mathrm{d}x}{d_p}. \tag{55}$$

It can be inferred from the equation above that the friction contribution to the overall change scales with $\kappa M^2 f$, and the heat exchange contribution with $\widetilde{Q}$. The friction coefficient is always positive, while the heating coefficient is positive in heating, and negative in cooling. Thus, friction

Table 5
Setups used in CFD-DEM simulations with heat exchange and friction.

Simulation	$\dot{Q}_p$ (W)	M_{in} (−)	M_{out} (−)	$\bar{f}$ (−)	$\bar{\widetilde{Q}}$ (−)
1	0.2	0.071	0.088	1.3	0.03
2	−0.1	0.030	0.027	1.5	−0.04
3	−0.1	0.035	0.040	14	−0.02

and heating add up with respect to a (negative) density change in the system, while cooling and friction counteract each other.

We define the ratio of a frictional to a heat-induced contribution as:

$$\varrho \equiv \frac{\kappa M^2 f}{\widetilde{Q}}. \tag{56}$$

Using a Runge-Kutta-based integration of Eq. (27) for different contribution ratios ϱ, we construct regime maps for flow with combined heat exchange and friction shown in Fig. 7. Thick dash-dotted lines represent the analytical boundaries for compressible frictionless flow (i.e., Eqs. (50) and (51)). In heating, friction shifts the boundary so that the compressible flow occurs sooner. However, in cooling, the density increase is counteracted by friction, delaying the onset of a compressible flow. The regime map based on the minimum Mach number (Fig. 7b) has additional dotted lines representing the chocking condition., at which the maximum Mach number reaches 1. Similar as before, adding friction to heated flow moves the onset of sonic flow to lower values of $\widetilde{Q}L/d_p$, while the opposite is true in the case of cooling.

Observing the flow at low Mach numbers, we can see that adding friction up to approximately $\varrho = 0.1$ does not significantly affect the criteria defined for frictionless flow in Eq. (54). Equal contribution of heat and friction ($\varrho = 1$) shifts the boundary for compressible limit from ≈ 0.2 to half of its value, i.e. ≈ 0.1.

Next, we show how adding friction affects the temperature change. Setting the change of the particle volume fraction to zero in Eq. (27), the differential temperature change is described by:

$$\frac{\mathrm{d}T}{T} = -\frac{\kappa(\kappa-1)M^4}{1-M^2} f \frac{\mathrm{d}x}{d_p} + \frac{1-\kappa M^2}{1-M^2} \widetilde{Q} \frac{\mathrm{d}x}{d_p}. \tag{57}$$

From the relation above, we notice that the frictional contribution to the temperature change is negative, meaning that friction causes the temperature to drop. The frictional contribution scales with M^4 which tends to zero for small velocities. The heat exchange contribution tends to

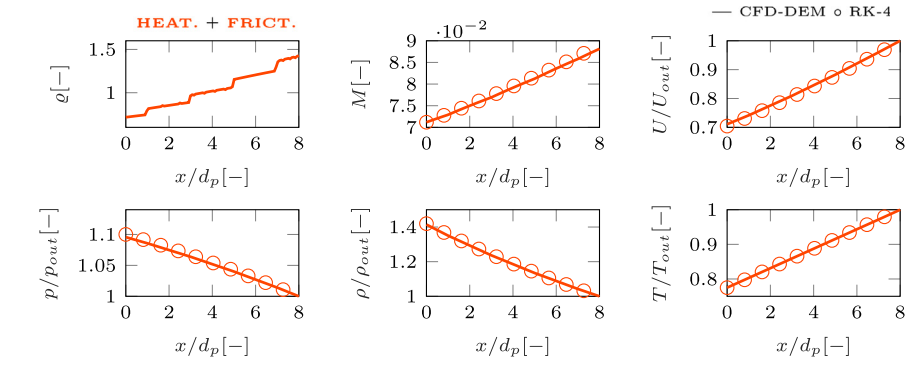

(a) Heated flow with friction

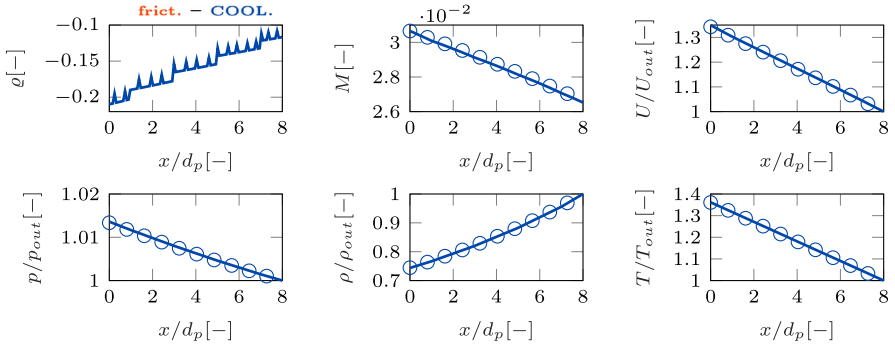

(b) Strongly cooled flow with friction

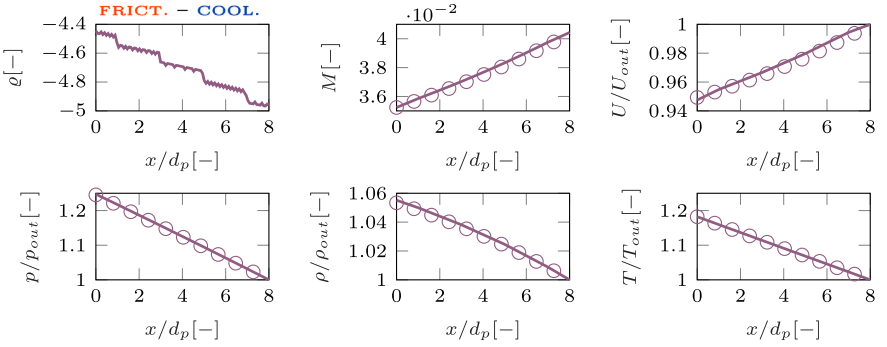

(c) Cooled flow with friction

Fig. 9. Changes of flow properties along the bed length in flow with heat exchange and friction.

zero for $M = 1/\sqrt{\kappa}$. We have shown that in frictionless flow, and for velocities in the Mach number range $1/\sqrt{\kappa}<M<1$, the temperature drops if the fluid is heated, and rises if the fluid is cooled. Similar as before, we derive a dimensionless contribution coefficient as:

$$\varrho_T \equiv \frac{\kappa(\kappa-1)M^4 f}{|1-\kappa M^2|\tilde{Q}}. \tag{58}$$

However, to keep the above coefficient constant in the entire subsonic range, the friction factor would have to become very large at low velocities. Thus, to show how the addition of friction affects the boundaries of the non-isothermal flow region, we will use ϱ given by Eq. (56). The resulting maps shown in Fig. 8 indicate that adding friction does not significantly affect the non-isothermal flow boundaries, meaning that criteria for isothermal and non-isothermal flow from Eq. (54) remains valid. However, as we have already shown, friction does greatly affect the velocity field, consequently shifting the transition to sonic flow to occur sooner in the case of heating, and later in the case of in cooling.

Finally, to illustrate how flow properties change in the flow with friction and heat exchange, we compared the Runge-Kutta-based solution to the results of CFD-DEM simulations. We run simulations based on parameters given in Table 5.

We used the following boundary conditions: $p_{out} = 10^5$Pa, $U_{\text{in}} = 10\frac{\text{m}}{\text{s}}$, $T_{in} = T_p = 1000$K, $L/d_p = 20$, and considered the geometry as in shown in Fig. 2a. Results for simulation setup 1, shown in Fig. 9a, show that friction and heating add up to higher compressibility effects. For simulation setup 2 (Fig. 9b), cooling overpowers friction ($|\varrho| < 1$), causing velocity and temperature to drop. In simulation setup 3 (Fig. 9c), cooling and friction are in the same scale of magnitude ($|\varrho| > 1$). Thus, the flow remains incompressible: velocity and density experience only small changes. For all three simulation setups, the maximum relative error stayed below 1% between the Runge-Kutta-based solution and our CFD-DEM simulations. The mean relative error for all three simulations was 0.14%.

3.5. Flow with change in particle volume fraction

We construct a regime map showing regions of compressible and incompressible flow, for one-dimensional flow featuring a linear change of particle volume fraction in a static packed bed. Additionally, we show that such flow can be considered as effectively isothermal. Depending on whether the particle volume fraction is decreasing or increasing in the flow direction, the flow will have properties as summarized in Table 6.

Using Eq. (36), the density ratio $\rho_{in}/\rho_{out} = \delta_\rho$ can be related to the outlet or the inlet state, resulting respectively in:

$$\frac{A_{\text{out}}}{A_{\text{in}}} = \tilde{C}\frac{L}{d_p} + 1 \quad = \delta_\rho \cdot \sqrt{\frac{\frac{\kappa-1}{2}M_{\text{out}}^2 + 1 - \delta_\rho^{\kappa-1}}{\frac{\kappa-1}{2}M_{\text{out}}^2}}, \tag{59}$$

Table 6
Properties of frictionless flow with linear change in particle volume fraction.

	Nozzle	Diffuser
Normalized slope of voidage change	$\tilde{C}<0$	$\tilde{C}>0$
Maximum Mach number	$M_{max} = M_{out}$	$M_{max} = M_{in}$
Minimum Mach number	$M_{min} = M_{in}$	$M_{min} = M_{out}$
Compressible flow limit	$\delta_\rho = 1.25$	$\delta_\rho = 0.75$
Incompressible flow limit	$\delta_\rho = 1.1$	$\delta_\rho = 0.9$

or

$$\frac{A_{\text{out}}}{A_{\text{in}}} = \tilde{C}\frac{L}{d_p} + 1 = \sqrt{\frac{\frac{\kappa-1}{2}M_{\text{in}}^2 \cdot \delta_\rho^{\kappa+1}}{\delta_\rho^{\kappa-1}\left(\frac{\kappa-1}{2}M_{\text{in}}^2 + 1\right) - 1}}. \tag{60}$$

These relations are defined only for values of δ_ρ which give positive parameters of the square root function. Using the properties from Table 6 in Eqs. (59) and (60), we construct regime maps described with the maximum and the minimum Mach number, shown respectively in Fig. 10a and b. The boundaries of the incompressible region are represented with light blue dashed lines, while the dark blue dashed lines represent the boundaries of the compressible region. The map linked to the minimum Mach number has additional continuous lines denoting the sonic flow, i.e., using $M_{max} = 1$ in Eq. (36).

To test the validity of the isothermal flow assumption, we express Eq. (36) in terms of the temperature ratio and the outlet or the inlet Mach number, leading to respectively:

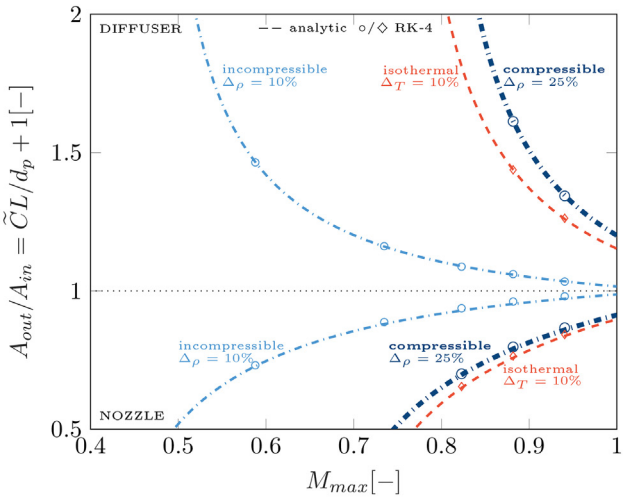

(a) based on the maximum Mach number

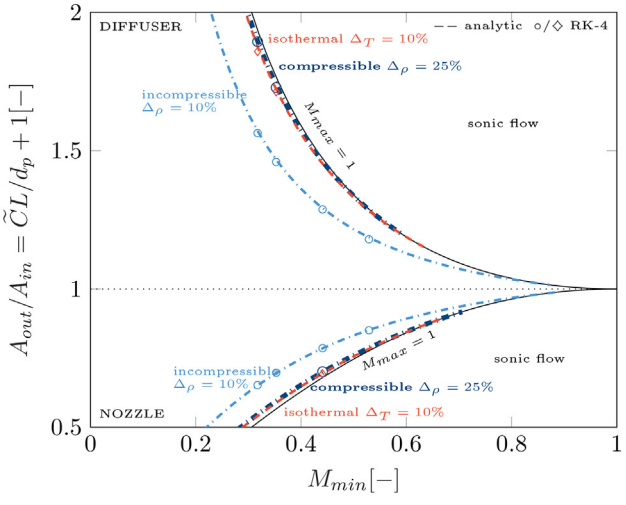

(b) based on the minimum Mach number

Fig. 10. Regime map for frictionless flow with linear change in particle volume fraction.

$$\frac{A_{\text{out}}}{A_{\text{in}}} = \tilde{C}\frac{L}{d_p} + 1 \quad = \delta_T^{\frac{1}{\kappa-1}} \sqrt{\frac{\frac{\kappa-1}{2}M_{\text{out}}^2 + 1 - \delta_T}{\frac{\kappa-1}{2}M_{\text{out}}^2}}, \tag{61}$$

and

$$\frac{A_{\text{out}}}{A_{\text{in}}} = \tilde{C}\frac{L}{d_p} + 1 \quad = \sqrt{\frac{\frac{\kappa-1}{2}M_{\text{in}}^2}{\delta_T\left(\frac{\kappa-1}{2}M_{\text{in}}^2 + 1\right) - 1}\,\delta_T^{\frac{\kappa+1}{\kappa-1}}}. \tag{62}$$

The value under a square root must be non-negative, leading to the following condition:

$$\frac{1}{\left(\frac{\kappa-1}{2}M_{\text{in}}^2 + 1\right)} < \delta_T < \frac{\kappa-1}{2}M_{\text{out}}^2 + 1 \tag{63}$$

Using the choking condition $M_{in} = M_{max} = 1$ and $M_{out} = M_{max} = 1$ in the above expression yields $0.83 < \delta_T < 1.2$. This means that the flow with a change in voidage can be effectively considered isothermal, if we adopt a relative temperature change of 25% to be the limit for non-isothermal flow according to Eq. (4). Thus, we expand the regime map using isothermal flow limits from Table 6 in Eqs. (61) and (62), plotted in light red in Fig. 10.

The range of the ordinate in Fig. 10 is determined by the possible range of particle volume fractions: from zero (i.e., no particles) to the maximum packing density, which amounts to approximately 50% of the cross-section for identical spherical particles. The corresponding maximum voidage is at the cross-section devoid of particles: $A_{\max} \equiv \left(1-\varphi_p\right)_{\max} = 1$. The minimum voidage is at the cross-section having the maximum packing density, i.e., the cross section approximately half-filled with particles: $A_{\min} \equiv \left(1-\varphi_p\right)_{\min} = 0.5$. Therefore, in the nozzle flow configuration, where the flow is towards an increasing particle volume fraction, the maximum change of the available area amounts to: $A_{\text{out}}/A_{\text{in}} = \left(1-\varphi_p\right)_{\min}/\left(1-\varphi_p\right)_{\max} = 0.5$. In the diffuser flow configuration, where the flow is in the direction of decreasing particle volume fraction, the maximum change of the available area amounts to: $A_{\text{out}}/A_{\text{in}} = \left(1-\varphi_p\right)_{\max}/\left(1-\varphi_p\right)_{\min} = 2$.

Fig. 10 reveals that a change in particle volume fraction will cause compressible flow only at extremely high Mach numbers, i.e., near transonicity. In the diffuser flow, the 10% temperature change occurs before the compressible flow limit (i.e., density change of 25%), while the opposite occurs in the nozzle flow. Regime map based on the minimum Mach number, shown in Fig. 10b, indicates that both the isothermal flow and the compressible flow limit tend to co-occur with the sonic flow condition $M_{max} = 1$.

3.6. Flow with change in particle void fraction and friction

To accurately represent gas-particle systems, we cannot neglect friction due to gas-particle drag. Thus, we are interested to see how adding friction affects compressibility in a bed with variable particle volume fraction, i.e. variable voidage. Setting the heat exchange coefficient to zero in Eq. (27), the differential change in gas density is as follows:

$$\frac{\mathrm{d}\rho}{\rho} = -\frac{\kappa M^2}{1-M^2} f\frac{\mathrm{d}x}{d_p} + \frac{M^2}{1-M^2}\frac{\mathrm{d}A}{A} = -\frac{\kappa M^2}{1-M^2} f\frac{\mathrm{d}x}{d_p} + \frac{M^2}{1-M^2}\frac{\tilde{C}}{1+\tilde{C}\frac{x}{d_p}}\frac{\mathrm{d}x}{d_p}. \tag{64}$$

In the equation above, the friction contribution scales with κf, and the contribution due to linear variation in particle volume fraction with $-\widetilde{C}/\left(1+\widetilde{C}x/d_p\right)$. While the friction coefficient is always positive, the particle volume fraction can decrease or increase. In nozzle flow, friction in conjunction with the converging cross-section $\widetilde{C}<0$ will add up to enhance compressibility in the system. In diffuser flow, friction will counteract the changes due to the diverging cross-section $\widetilde{C}>0$ reducing the density change.

We define the ratio of a friction to voidage change contribution as follows:

$$\varpi \equiv \frac{f\kappa}{|\widetilde{C}|/\left(1+|\widetilde{C}|L/d_p\right)}. \tag{65}$$

Using Runge-Kutta-based numerical integration of Eq. (27) for different contribution ratios ϖ, we construct regime maps for the flow with combined change of voidage and friction as shown in Fig. 11.

The thick dash-dotted lines represent the analytical limits for compressible frictionless flow, Eqs. (59) and (60). Adding friction to a nozzle-like flow shifts the compressible flow limit towards lower changes in particle volume fraction, widening the compressible region. In diffuser-like flow, friction shifts the compressibility limit towards higher velocities and higher changes in particle volume fraction.

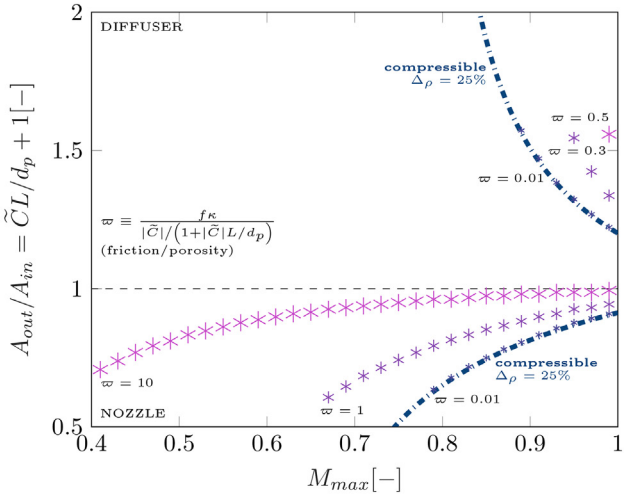

(a) based on the maximum Mach number

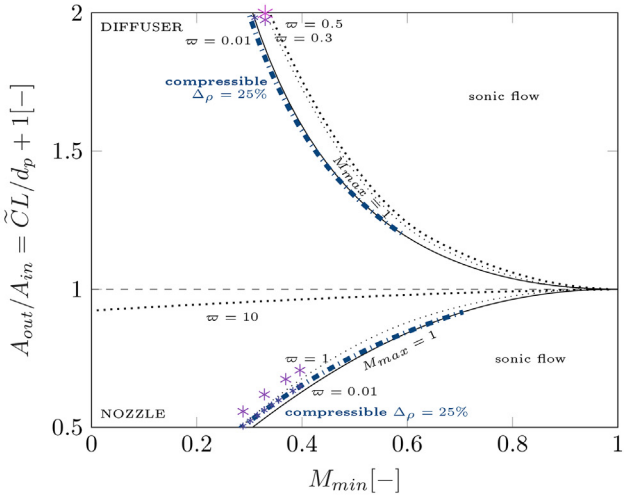

(b) based on the minimum Mach number

Fig. 11. Regime map with compressible flow regions in flow with friction and change in particle volume fraction.

The regime map based on the minimum Mach number (Fig. 11b) has additional dotted lines representing the chocking condition, i.e. where the corresponding maximum Mach number in the flow reaches unity. These lines delineate the sonic flow region. Similar as before, adding friction to the nozzle flow moves the onset of the sonic flow to lower values of particle volume fraction, while the opposite occurs in the diffuser flow. Boundaries of the compressible flow region coincide with the sonic flow boundaries. In the case of a nozzle flow with strong friction (i.e., $\varpi = 10$), the velocity change is greater than the density change, leading to a sonic flow before the density change reaches the 25% compressible flow limit.

According to Fig. 11, the compressible effects in diffuser flow are only observed close to the sonic boundary. Therefore, a frictional subsonic flow in the diffuser regime will not lead to significant density changes in the system, and can be treated as incompressible.

The flow in the nozzle regime is also compressible only at high Mach numbers, i.e., above approximately 0.1 with moderate friction.

Next, we take a look on how friction and a change in the particle volume fraction affect the isothermal limit $\Delta_T = 10\%$. Setting the heat exchange contribution in Eq. (27) to zero, the temperature change is as follows:

$$\begin{aligned}\frac{\mathrm{d}T}{T} &= -\frac{\kappa(\kappa-1)M^4}{1-M^2} f\frac{\mathrm{d}x}{d_p} + \frac{(\kappa-1)M^2}{1-M^2}\frac{\mathrm{d}A}{A} \\ &= -\frac{\kappa(\kappa-1)M^4}{1-M^2} f\frac{\mathrm{d}x}{d_p} + \frac{(\kappa-1)M^2}{1-M^2}\frac{\widetilde{C}}{1+\widetilde{C}\dfrac{x}{d_p}}\frac{\mathrm{d}x}{d_p}.\end{aligned} \tag{66}$$

In the equation above, the friction contribution scales with $\kappa f M^2$, and the contribution due to a linear change in particle volume fraction to $-\widetilde{C}/\left(1+\widetilde{C}x/d_p\right)$. Compared to the density change in Eq. (64), friction additionally scales with M^2. Hence, in subsonic flows, with $M < 1$, friction will contribute less to the temperature change than to the density change. We introduce the following dimensionless coefficient to illustrate the combined effect of friction and variable particle volume fraction on the overall temperature change:

$$\varpi_T \equiv \frac{f\kappa M^2}{|\widetilde{C}|/\left(1+|\widetilde{C}|L/d_p\right)}. \tag{67}$$

Using Runge-Kutta integration of Eq. (27) for different ϖ_T, we construct regime maps which show how adding friction affects the boundary of the isothermal flow region. The regime map based on the maximum Mach number (Fig. 12a) shows that the friction in conjunction with the increasing voidage in a diffuser flow suppresses the temperature change, expanding the isothermal region. In nozzle flow, friction and decreasing voidage add up, moving the isothermal boundary to lower velocities and reducing the isothermal region.

The regime map based on the minimum Mach number (Fig. 12b) has additional lines describing the sonic flow region. In diffuser flow, a 10% temperature change coincides with the sonic flow boundary. In nozzle flow with high friction, the velocity change is greater than the temperature change, generating sonic flow before the isothermal to non-isothermal transition is reached.

Finally, we show the results for a CFD-DEM simulation of a nozzle flow. The domain is as indicated in Fig. 2b, with particles stacked up so that they cover the entire outlet height. Following properties are considered: $L/d_p = 50[-]$, $H/d_p = 20[-]$, $p_{\text{in}} = 1000\text{Pa}$, $U_{\text{out}} = 200\frac{\text{m}}{\text{s}}$, $T_{\text{out}} = T_p = 500\text{K}$. These conditions add up to the following dimensionless parameters: $\left(1-\varphi_p\right)_{\text{out}}/\left(1-\varphi_p\right)_{\text{in}} = 0.54$, $M_{in} = 0.07$, $M_{out} = 0.16$, $\bar{f} = 1.3$, and $\widetilde{C} = -0.01$. The profiles of the system properties are shown in Fig. 13. The maximum relative error between CFD-DEM and Runge-Kutta solution reached 1.98%, while the mean relative error is 0.32%.

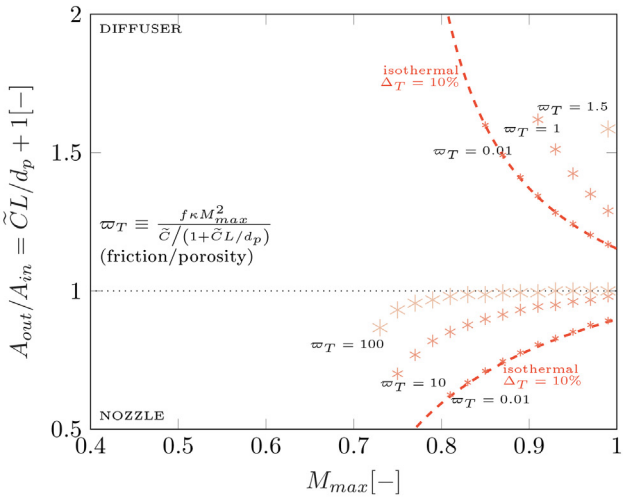

(a) based on the maximum Mach number

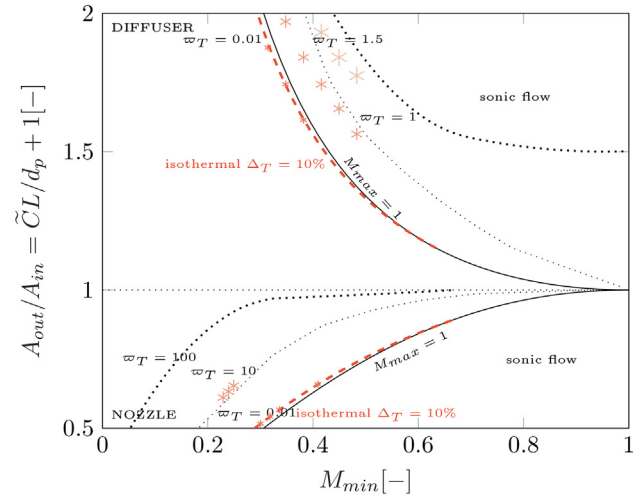

(b) based on the minimum Mach number

Fig. 12. Regime map with isothermal flow regions in flow with friction and change in particle volume fraction.

Since friction and converging cross-section add up to the same effect, we see the same behaviour as predicted in pure friction or pure nozzle flow: Mach number and velocity rise, while pressure, density, and temperature drop towards the outlet. As in flow with friction (but with constant particle volume fraction), no heat exchange leads to insignificant changes in temperature. It is important to recognize that friction contribution had to be very high ($\varpi > 100$) in order to induce compressible flow at such low Mach numbers ($M \approx 0.1$). This essentially proves that at low velocities changes in particle volume fraction do not contribute to changes in density. According to Eq. (42), the considered flow is compressible, regardless of the change in the particle volume fraction.

4. Conclusion

Traditionally, $M > 0.3$ is considered the ultimate indicator of a compressible flow. Gas-particle flows, which often occur at lower Mach numbers, are therefore almost always modelled as incompressible. And while the criterion holds true for a flow around a single sphere,

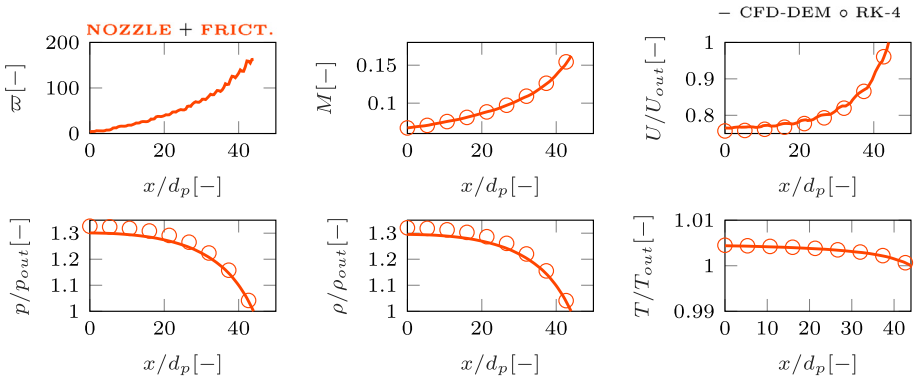

Fig. 13. Changes of flow properties along the bed length in flow with friction and increasing particle volume fraction.

drag forces that arise in assemblies of particles are such that compressible effects show already at much lower Mach numbers.

To determine the critical system parameters that onset a compressible flow, we examine factors connected to the compressibility of the gas: (i) friction (i.e., momentum transfer due to gas-particle drag), (ii) heat exchange, and (iii) a change of the particle volume fraction. For flows dominated by each of the aforesaid factors, we construct regime maps that demarcate regions of compressible and incompressible flow. We define the boundary of the compressible region to coincide with 25% relative change of density along the streamline. We consider the flow to be effectively incompressible for relative density changes below 10%. Additionally, we apply the same methodology to test the validity of the isothermal flow assumption.

Assuming velocities are deeply subsonic ($M < 0.1$), an adiabatic system will show compressibility if the following relations are true:

$$\left(5f\frac{L}{d_p}-\frac{1}{5}\right)M^2_{\max}>1,$$
$$\left(7.78f\frac{L}{d_p}-\frac{1}{5}\right)M^2_{\min}>1.$$

In the relations above, f is the friction coefficient of the system, L is the bed length, and d_p is the particle diameter. The maximum Mach number M_{max} will develop at the outlet, while the minimum Mach number characterizes the state at the inlet. Applying the above criterion to clustering in fluidized beds, we found systems with particle diameters of 1000μm affected. Dense systems ($\varphi_p > 0.3$) with particle diameters of 100μm at low pressures (1kPa) also displayed large changes in density.

For flows dominated by heat exchange, the criteria defined in the following equations can be applied to assess the flow regime at low Mach numbers ($M < 0.2$):

$$|\tilde{Q}|L/d_p<0.1 \quad \Rightarrow \text{the flow is incompressible and isothermal},$$
$$\tilde{Q}L/d_p>0.2 \quad \Rightarrow \text{the flow is heated, compressible, but isothermal},$$
$$\tilde{Q}L/d_p>0.3 \quad \Rightarrow \text{the flow is heated, compressible and non}-\text{isothermal},$$
$$\tilde{Q}L/d_p<-0.2 \quad \Rightarrow \text{the flow is cooled, non}-\text{isothermal, but incompressible},$$
$$\tilde{Q}L/d_p<-0.3 \quad \Rightarrow \text{the flow is cooled, compressible and non}-\text{isothermal},$$

where $\tilde{Q}$ is a dimensionless heating coefficient. The above compressibility-related limits are valid for systems with friction contributing up to $\varrho \equiv \kappa M^2 f/\tilde{Q} = 0.1$ (Eq. (56)). However, heated flow with friction and heat exchange in the same order of magnitude ($\varrho \approx 1$) will have the limit for compressible flow reduced to about 50%, i.e. compressible effects will already show at $\tilde{Q}L/d_p \approx 0.1$. Change in temperature can be significantly affected only by heat exchange. This means that the criteria for isothermal and non-isothermal flow in Eq. (54) holds regardless of friction in system.

Changes due to variations in particle volume fraction are insufficiently large to affect compressibility in a gas-particle system, and can be therefore neglected.

Compressible gas-particle flows can be calculated using CFD-DEM models. The model we presented is implemented in CFDEMCoupling [8,23]. We obtained good agreement between CFD-DEM solution and other numerical and analytical methods for flows up to $M = 0.1$. At such high velocities relative errors reach 5% at most, while for the velocities below the mean error stays below 1%. In future, specialized CFD-DEM simulation models are required to push these boundaries in terms of Mach number. In order to verify the correct implementation of such advanced compressible CFD-DEM formulations, the analytical and semi-analytical solutions presented by us might be extremely valuable.

Declaration of Competing Interest

The authors declare that they have no known competing financial interests or personal relationships that could have appeared to influence the work reported in this paper.

Acknowledgements

This project is funded through Marie SKŁODOWSKA-CURIE Innovative Training Network **MATHEGRAM**, the People Programme (Marie SKŁODOWSKA-CURIE Actions) of the European Union's Horizon 2020 Programme H2020 under REA grant agreement No. 813202.

References

[1] E. Muschelknautz, W. Krambrock, Vereinfachte Berechnung horizontaler pneumatischer Förderleitungen bei hoher Gutbeladung mit feinkornigen Produkten, Chem. Ing. Tech. 41 (1969) 1164–1172.
[2] K. Konrad, Dense-phase pneumatic conveying through long pipelines: effect of significantly compressible air flow on pressure drop, Powder Technol. 48 (1996) 193–203.
[3] A. Srivastava, K. Agrawal, S. Sundaresan, S.B.R. Karri, T.M. Knowlton, Dynamics of gas-particle flow in circulating fluidized beds, Powder Technol. 100 (1998) 173–182.
[4] S.B.R. Karri, A. Issangya, T.M. Knowlton, Gas bypassing in deep fluidized beds, Fluidization XI, Engineering Conferences International, 2004.
[5] T. Li, J. Grace, L. Shadle, C. Guenther, On the superficial gas velocity in deep gas-solids fluidized beds, Chem. Eng. Sci. 66 (2011) 5735–5738.
[6] M. Salehi, M. Askarishahi, S. Radl, Analytical solution for thermal transport in packed beds with volumetric heat source, Chem. Eng. J. 316 (2017) 131–136.
[7] S.A. Metel, M.M. Stebulyanin, S.V. Fedorov, A.A. Okunkova, Power density distribution for laser additive manufacturing (SLM): potential, fundamentals and advanced applications, Technologies 7 (2019) 5.
[8] C. Goniva, C. Kloss, N. Deen, J.A.M. Kuipers, S. Priker, Influence of rolling friction modelling on single spout fluidized bed simulations, Particuology 10 (2012) 582–591.
[9] T.B. Anderson, R. Jackson, A fluid mechanical description of fluidied beds, I&EC Fundam. 6 (1967) 527–539.

[10] J. Tausendschön, J. Kolehmainen, S. Sundaresan, S. Radl, Coarse graining Euler-Lagrange simulations of cohesive particle fluidization, Powder Technol. (2020) https://doi.org/10.1016/j.powtec.2020.01.056.
[11] S. Kuang, K. Li, A. Yu, CFD-DEM simulation of large-scale dilute-phase pneumatic conveying system, Ind. Eng. Chem. Res. (2019) https://doi.org/10.1021/acs.iecr.9b03008.
[12] K. Shimura, A. Matsuo, Using an extended CFD-DEM for the two-dimensional simulation of shock-induced layered coal-dust combustion in a narrow channel, Proc. Combust. Inst. 37 (2019) 3677–3684.
[13] L.R. Glicksman, Scaling relationships for fluidized beds, Chem. Eng. Sci. 39 (1984) 1373–1379.
[14] M. Rüdisüli, T.J. Schildhauer, S.M.A. Biollaz, J.R. van Omen, Scale-up of bubbling fluidized bed reactors – a review, Powder Technol. 217 (2011) 21–38.
[15] P.H. Oosthuizen, W.E. Carscallen, Compressible Fluid Flow, McGraw-Hill, 1997.
[16] T.G. Theofanous, C.-H. Chang, The dynamics of dense particle clouds subjected to shock waves: Part 2. Modeling/numerical issues and the way forward, Int. J. Multiphase Flow 89 (2017) 177–206.
[17] Y. Mehta, C. Neal, K. Salari, T.L. Jackson, S. Balachandar, S. Thakur, Propagation of a strong shock over a random bed of spherical particles, J. Fluid Mech. 839 (2018) 157.
[18] G.S. Shallcross, R.O. Fox, J. Capecelatro, A volume-filtered description of compressible particle-laden flows, Int. J. Multiphase Flow 122 (2020) https://doi.org/10.1016/j.ijmultiphaseflow.2019.103138.
[19] S.K. Lele, Flows with density variations and compressibility: similarities and differences, IUTAM Symposium on Variable Density Low-Speed Turbulent Flows, Springer 1997, pp. 279–301.
[20] R.D. Zucker, O. Biblarz, Fundamentals of Gas Dynamics, John Wailey & Sons, 2002.
[21] S. Ergun, Fluid flow through packed columns, Chem. Eng. Prog. 48 (1952) 89–94.
[22] D.J. Gunn, Transfer of heat or mass to particles in fixed and fluidised beds, Int. J. Heat Mass Transf. 21 (1978) 467–476.
[23] CFDEMcoupling Open Source CFD-DEM Framework, (2021). https://www.cfdem.com/cfdemrcoupling-open-source-cfd-dem-framework (accessed 27.01.21).
[24] C. Kloss, C. Goniva, A. Hager, S. Amberger, S. Priker, Models, algorithms and validation for open source DEM and CFD-DEM, Prog. Comput. Fluid Dyn. 12 (2012) 140–152.
[25] LIGGGHTS Open Source DEM Particle Simulation Code, (2021) https://www.cfdem.com/liggghts-open-source-discrete-element-method-particle-simulation-code (accessed 27.01.21).
[26] H.G. Weller, G. Tabor, H. Jasak, C. Fureby, A tensorial approach to computational continuum mechanics using object oriented techniques, Comput. Phys. 12 (1998) 620–631.
[27] C.J. (2018). Greenshields, OpenFOAM User Guide, The OpenFOAM Foundation.
[28] OpenFOAM v6 C++ Source Guide, (2018). https://cpp.openfoam.org/v6/ (accessed 27.01.21).
[29] Z.Y. Zhou, S.B. Kuang, K.W. Chu, A.B. Yu, Discrete particle simulation of particle-fluid flow: model formulations and their applicability, J. Fluid Mech. 661 (2010) 482–510.
[30] H.R. Norouzi, R. Zarghami, S.-G.R., N. Mostoufi, Coupled CFD-DEM Modeling: Formulation, Implementation and Application to Multiphase Flows, Wiley, 2016.
[31] R.W. Houim, E.S. Oran, A multiphase model for compressible granular-gaseous flows: formulation and initial tests, J. Fluid Mech. 789 (2016) 166.
[32] B.H. Xu, A.B. Yu, Numerical simulation of the gas-solid flow in a fluidized bed by combining discrete particle method with computational fluid dynamics, Chem. Eng. Sci. 52 (1997) 2785–2809.
[33] CFDEMcoupling Documentation: Divided Void Fraction Command, (2016). https://www.cfdem.com/media/CFDEM/docu/voidFractionModel_dividedVoidFraction.html (accessed 17.06.21).
[34] D.L. Koch, R.J. Hill, Inertial effects in suspension and porous-media flows, Annu. Rev. Fluid Mech. 33 (2001) 619–647.
[35] R. Di Felice, The voidage function for fluid-particle interaction systems, Int. J. Multiphase Flow 20 (1994) 153–159.
[36] D. Gidaspow, Multiphase Flow and Fluidization: Continuum and Kinetic Theory Descriptions, Academic Press, 1994.
[37] C.B. Henderson, Drag coefficients of spheres in continuum and rarefied flows, AIAA J. 14 (1976) 707–708.
[38] E. Loth, Compressibility and rarefaction effects on drag of a spherical particle, AIAA J. 46 (2008) 2219–2228.
[39] M. Parmar, A. Haselbacher, S. Balachandar, Improved drag correlation for spheres and application to shocktube experiments, AIAA J. 48 (2010) 1273–1277.
[40] Y. Mehta, C. Neal, T.L. Jackson, S. Balachandar, S. Thakur, Shock interaction with three-dimensional face centered cubic array of particles, Phys. Rev. Fluids 1 (2016) 157.
[41] M. Askarishahi, M. Salehi, S. Radl, Voidage correction algorithm for unresolved Euler-Lagrange simulations, Comput. Part. Mech. 5 (2018) 607–625.
[42] L. Schiller, A. Naumann, A drag coefficient correlation, Z. Ver. Dtsch. Ing. 77 (1935) 318–320.
[43] S. Sundaresan, S. Radl, C.C. Milioli, F.E. Milioli, Coarse-grained models for momentum, energy and species transport in gas-particle flows, Proceedings of the 14th International Conference on Fluidization – From Fundamentals to Products, ECI Symposium Series, 2013.
[44] S. Schneiderbauer, P. Fede, O. Simonin, Turbulent length scales in unbounded fluidization, Proceedings of the 10th International Conference on Multiphase Flow, Rio de Janeiro, Brazil, 2019.
[45] R. Beetstra, M.A. van der Hoef, J.A.M. Kuipers, Drag force of intermediate Reynolds number flow past mono- and bidisperse arrays of spheres, AIChE J. 53 (2007) 489–501.